Contributions to Mineralogy and Petrology (2018) 173:33
https://doi.org/10.1007/s00410-018-1459-0

ORIGINAL PAPER

Evacuation of multiple magma bodies and the onset of caldera collapse in a supereruption, captured in glass and mineral compositions

Elliot J. Swallow[1] · Colin J. N. Wilson[1] · Madison L. Myers[2] · Paul J. Wallace[2] · Katie S. Collins[1,3] · Euan G. C. Smith[1]

Received: 6 August 2017 / Accepted: 27 March 2018 / Published online: 29 March 2018

Abstract

Complexities in the nature of large-scale silicic eruptions and their magmatic systems can be discerned through micro-analytical geochemical studies. We present high-resolution, stratigraphically constrained compositional data on glassy matrix material and feldspar crystals from the initial fall deposits and earliest ignimbrite (base of member A) of the 2.08 Ma, ~2500 km^3 Huckleberry Ridge Tuff (HRT), Yellowstone. We use these data to document the nature of the magmatic system and compositional changes related to the transition from fall to widespread ignimbrite deposition, inferred to mark the onset of caldera collapse. Although major element glass compositions are relatively uniform, trace elements span a large range (e.g. Ba 10–900 ppm, Sr/Rb = 0.005–0.09), with highly evolved glasses dominating in the fall deposits. Several trace elements (e.g. Ba and light rare earth elements) in the glass samples serve to define statistically significant compositional clustering in the fall deposits and basal ignimbrite. These clusters are inferred to reflect melt compositions controlled by fractional crystallisation processes and are interpreted to represent multiple, discrete melt-dominant domains that were tapped by multiple vents. The onset of widespread ignimbrite deposition is marked by an increase in the number of erupted melt compositional clusters from four in the fall deposits to eight, representing nine melt-dominant domains. There is an absence of geographical variation of glass compositions within the basal ignimbrite, with samples from proximal to distal localities north, west and south of the HRT caldera exhibiting similar variability. Pairing of glass analyses with sanidine major and minor element compositional data suggests that the nine melt compositional domains converged at depth into two compositionally distinct upper-crustal magmatic lineages that were both active during these early stages of the eruption. Our data collectively indicate the evacuation of an exceptionally complex and heterogeneous magma system. The onset of widespread ignimbrite deposition, inferred to relate to caldera collapse, occurred after ~ 50 km^3 of magma had been discharged. Although external controls were important as an eruption trigger, depressurisation of the system led to caldera collapse with the eruption of numerous discrete melt-dominant domains.

Keywords Huckleberry Ridge Tuff · Yellowstone · Supereruption · Caldera collapse · Glass compositions · Multiple magma bodies

Introduction

The explosive evacuation of large volumes of silicic magma represents the culmination of growth of crustal magma bodies and their release in catastrophic eruptions, at one extreme

Communicated by Gordon Moore.

Electronic supplementary material The online version of this article (https://doi.org/10.1007/s00410-018-1459-0) contains supplementary material, which is available to authorized users.

✉ Elliot J. Swallow
elliot.swallow@vuw.ac.nz

[1] School of Geography, Environment and Earth Sciences, Victoria University, PO Box 600, Wellington 6140, New Zealand

[2] Department of Earth Sciences, University of Oregon, Eugene, OR 97403-1272, USA

[3] Department of the Geophysical Sciences, University of Chicago, Chicago, IL 60637, USA

those termed supereruptions with $> 10^{15}$ kg of magma ejected (Miller and Wark 2008). Observations of historic events and studies of eruption products have long demonstrated that three transitions are common to ubiquitous in large explosive eruptions:

1. from initial, buoyant plume activity (yielding fall deposits) into column collapse (yielding ignimbrite: e.g. Wilson et al. 1980; Sparks et al. 1997);
2. from a single vent to multiple vents accompanying the onset of caldera collapse due to depressurisation of the system (e.g. Hildreth and Mahood 1986; Suzuki-Kamata et al. 1993); and
3. from compositional uniformity into coherent diversity as different levels of a zoned unitary chamber are sequentially tapped (e.g. Bacon and Druitt 1988; Schuraytz et al. 1989; Hildreth and Fierstein 2012; Bachmann et al. 2014).

These transitions, collectively exemplified by the Mazama eruption (Bacon 1983; Suzuki-Kamata et al. 1993), involve a transition from initial fall activity from a single vent that causes depressurisation of a unitary, compositionally stratified magma chamber, leading directly to caldera collapse and widespread ignimbrite deposition sourced from multiple vents along ring fractures. However, in other large eruptions, particularly of crystal-rich magmas, one or more of these transitions appear to be absent (e.g. Fish Canyon: Bachmann et al. 2002; Cerro Galan: Cas et al. 2011; Ongatiti: Cooper and Wilson 2014). The presence, ordering and nature of these transitions and their development with respect to the elapsed time into the eruption or volume of magma erupted yield important insights into the pre-eruptive state of the sub-surface magma body or bodies, and the mechanisms of eruption initiation and magma release.

Although these proposed transitions are straightforward and readily explained and modelled, there is debate centred on each aspect, together with the influences on eruption onset. Multiple factors have been proposed for eruption triggering, both internal, such as large mass influx (which may also lead to volatile exsolution), vigorous convection and buoyancy-generated overpressures (Caricchi et al. 2014; Degruyter and Huber 2014; Malfait et al. 2014), and external, such as roof destabilisation (Gregg et al. 2012) and tectonic forces (Allan et al. 2012; Myers et al. 2016). The balance between internal and external factors may reflect the magma body size (Gregg et al. 2015), as numerical models imply that smaller and larger bodies will exhibit contrasting behaviour and require different trigger mechanisms (Jellinek and DePaolo 2003; Gregg et al. 2012).

In turn, the timing and mechanisms of caldera collapse and associated widespread ignimbrite deposition, with or without generation of a preceding fall deposit, are also debated (e.g. Roche and Druitt 2001; Gregg et al. 2012; Cashman and Giordano 2014). Field evidence shows that in some eruptions the relationship between caldera collapse and eruptive dynamics is more complex than can be simply modelled. For example, in the Bishop Tuff, fall and flow deposition were coeval through most (if not all) of the eruption (Wilson and Hildreth 1997) and began prior to large-scale caldera collapse, the latter as inferred from changes in the lithic lithologies in the deposits (Hildreth and Mahood 1986).

Below the surface, models have predominantly focused on a single, unitary zoned magma body, with the accompanying view that the magmas ejected need be closely linked physically and/or compositionally and/or thermally (Hildreth 1981; Bacon and Druitt 1988; Singer et al. 2016). Field and geochemical data indicate that although this may be the case for some events (e.g. Mazama: Bacon 1983; Bacon and Druitt 1988; Novarupta: Hildreth and Fierstein 2012; Oruanui: Allan et al. 2017), others show the simultaneous or sequential tapping of multiple adjacent magma chambers in single or paired events (see Cashman and Giordano 2014 for overview). Published examples include the systematic involvement of separate large-scale magma bodies into a single caldera-forming event (e.g. Cooper et al. 2012, 2016), tectonically linked sequential eruption of two independent magma systems from separate vent areas (e.g. Nairn and Kohn 1973; Gravley et al. 2007; Bégué et al. 2014) and the 'accidental' involvement of magma from an independent magmatic system into a large caldera-forming eruption (e.g. Allan et al. 2012). These kinds of scenarios, because of their possible complexity, have seldom been incorporated into numerical models, and therefore the role of multiple magma bodies in the dynamics of single eruptions has not been fully explored (Gudmundsson 2012).

Here we consider the three transitions listed above and show how the possible complexities in large-scale magmatic systems are reflected during the early stages of an archetypal silicic supereruption. We document products of early eruptive stages of the Huckleberry Ridge Tuff (HRT: Christiansen 2001), the second largest Quaternary eruption on Earth. Although generally treated as conforming to the conventional view given above (e.g. Hildreth 1981; Hildreth et al. 1984, 1991; Christiansen 2001), our work shows a contrasting picture. A study of quartz-hosted melt inclusions and reentrants, and obsidian pyroclasts from its lowest fall layers (Myers et al. 2016) proposed that the earliest stages of the HRT eruption occurred from three compositionally distinct cupolas, erupting spasmodically in an overlapping sequence. We build on this work using samples of glassy matrix materials to document melt compositions through the entire thickness of the initial fall deposits and across the transition into the earliest ignimbrite. We show how the compositional diversity in the earliest fall deposits further

develops into an extraordinary degree of complexity in the ignimbrite. This complexity reflects the pre-eruptive configuration of the HRT magma system and illustrates the style of, and controls on, the onset of caldera collapse in this event.

Geological background

The ~2.08 Ma HRT supereruption is the earliest and largest (2500 km^3) of three caldera-forming eruptions at the Yellowstone Plateau volcanic field (YPVF; Christiansen 2001; Singer et al. 2014). The HRT consists of initial fall deposits overlain by three ignimbrite units (members A, B and C), together with additional, but more localised, fall deposits between members B and C (Christiansen 2001). The overall ~95 × 65 km HRT caldera is of irregularly ovoid shape. Within it, three vent foci for the three ignimbrite members were proposed by Christiansen (2001), but it is not established when and how the overall caldera structure developed during the eruption.

The initial fall deposits, particularly at the Mount Everts section studied by Myers et al. (2016), consist of multiple bedded layers, many of which are normally graded to fine-ash tops, indicating that the eruption was episodic in its early stages. This inference is reinforced at this locality and elsewhere by evidence for minor reworking at several horizons, particularly in the earliest fall deposits, interpreted to reflect short-term hiatuses that collectively represent a period of days to weeks. Once ignimbrite deposition commenced, however, only rarely are flow unit boundaries seen (most commonly within 1–3 metres of the basal contact), and no traces of erosional hiatuses are present within ignimbrite member A. The onset of ignimbrite A deposition appears to have been in close succession at locations situated > 180 km apart and on opposite sides of the caldera. We thus infer that the base of ignimbrite A reflects the onset of column collapse, the start of energetic, voluminous pyroclastic flow activity, and hence the beginning of caldera collapse (e.g. Wilson et al. 1980; Rosi et al. 1996).

Samples and analytical methods

Samples of glassy material and co-erupted (glass-coated) feldspar crystals were collected from eighteen horizons through the entire thickness of the initial fall deposits at the same location as Myers et al. (2016), a site north of the inferred eruptive source on the western rim of Mt. Everts near Mammoth, Wyoming (Fig. 1; Supplementary Fig. 1). The upper part of the fall deposits (top 1/3) is locally fused by the overlying ignimbrite, and the glass is darkened through microlite growth; although this material is studied here, it was not analysed by Myers et al. (2016) because the quartz-hosted melt inclusions were devitrified. Within the fall deposits, pumices are almost entirely < 1 cm long and hence unsuitable for individual clast analysis. We therefore sampled both the fragmented pale glass shards and co-erupted sparse (< 0.1% by volume) ash-grade fragments of black obsidian. The latter still contain appreciable amounts of CO_2 (20–50 ppm) and are hence inferred to be juvenile material rather than recycled earlier-erupted dome material (Myers et al. 2016; Watkins et al. 2017).

Glassy samples were also collected from the base of ignimbrite A from 17 localities across a 180° sector around the caldera (Fig. 1; Supplementary Table 1). Sampled materials include matrix shards from non-welded ignimbrite, fragments of basal vitrophyre, and glass kernels extracted from fiamme within the basal vitrophyre. Feldspar crystals from selected basal ignimbrite samples at a range of sites were also analysed. All samples were crushed, sieved, and glass and crystals picked, mounted into 1-inch epoxy mounts and polished.

Glass and crystals were analysed at Victoria University of Wellington for major elements by Electron Microprobe (EPMA) using a JEOL JXA-8230 SuperProbe and for trace elements by Laser-Ablation Inductively Coupled Plasma Mass Spectrometry (LA-ICP-MS) using a RESOlution S155-SE 193 nm Excimer Laser coupled with an Agilent 7500CS ICP–MS. Glass and obsidian shards were analysed by EPMA using a 15 kV accelerating voltage and a 20 µm spot size. Si, Al, Na, K, Fe Ca were analysed using a 2 nA beam current as recommended by Humphreys et al. (2006) to minimise alkali migration. Si and Na were analysed first to further reduce electron-beam effects. Ti, Mg and Mn were subsequently analysed using an 8 nA current. Count times on peak were 15 (Na), 30 (Si, Al), 40 (K, Ca, Ti, Mg) and 60 s (Fe, Mn). For EPMA analysis of feldspar, an accelerating voltage of 15 kV, a sample current of 12 nA, a spot size of ~1 µm and a 30 s count time on peak were used for all elements. LA–ICP–MS analysis of glass was conducted using a 35 µm spot size. Each analysis was preceded by two 70 µm cleaning pulses. ^{29}Si was used as an internal standard, GSD-1G for calibration and BHVO-2G, BCR-2G and NIST612 used as secondary standards.

Results

Major element compositions of glasses and feldspar

All glass and obsidian shards from the fall deposits and basal ignimbrite are high silica rhyolite (75.5–78.0 wt% SiO_2, normalised to 100% anhydrous: Electronic Appendix 1) and show major element trends broadly consistent with the crystallisation of the major and minor mineral phases present in the deposits (quartz, sanidine, plagioclase, clinopyroxene, Fe-rich olivine, Fe–Ti oxides: Fig. 2). Glass compositions

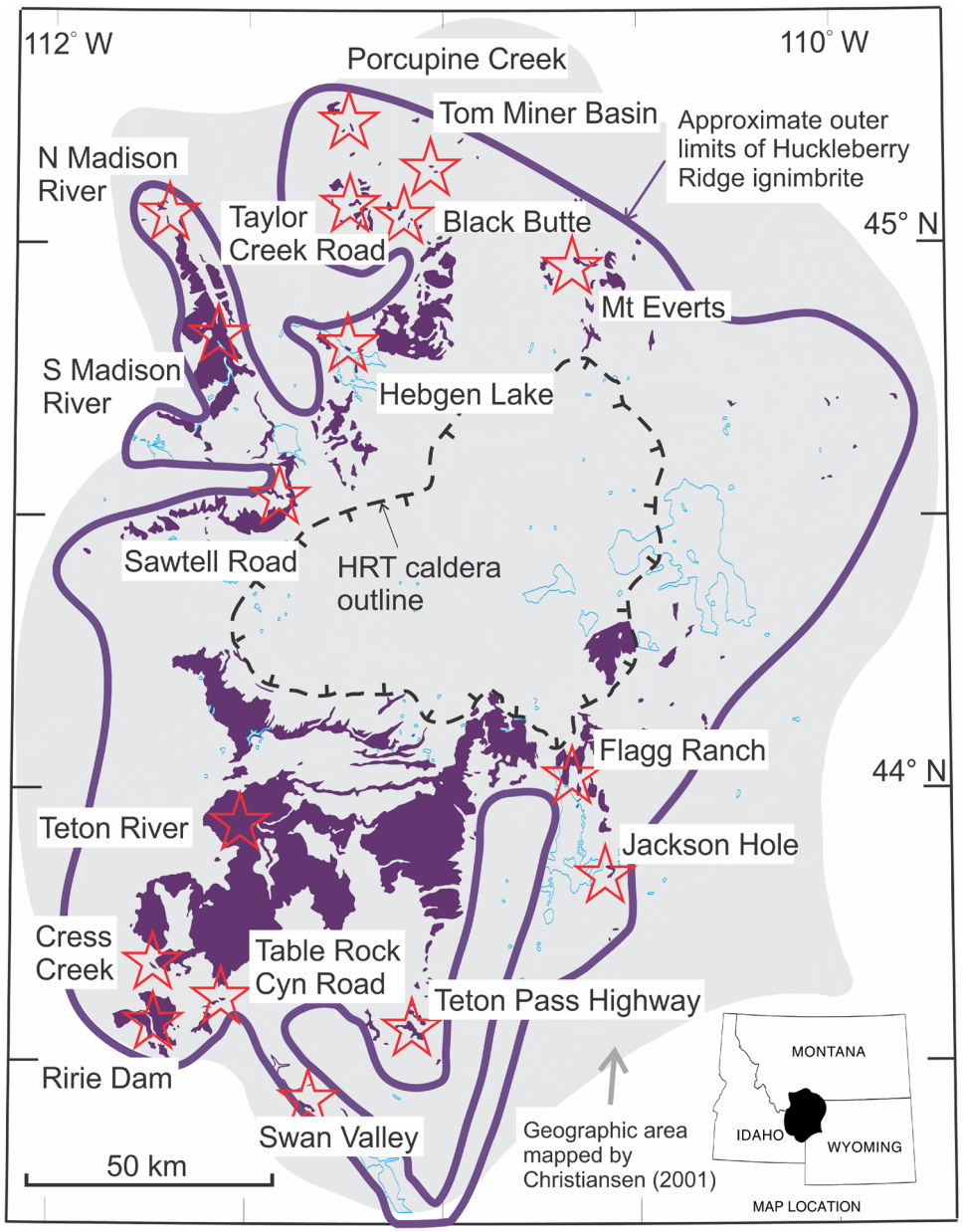

Fig. 1 Map of outcrop areas of the HRT ignimbrite (purple regions) and the inferred original extent of the ignimbrite (purple line). Red stars indicate locations where the basal ignimbrite was sampled. Further location details are given in Supplementary Table 1. HRT outcrop areas and caldera outline from Christiansen (2001)

within the fall deposits show little major element variation (SiO_2: 76.3–78.0 wt%, CaO: 0.46–0.63 wt%). Samples from the basal ignimbrite extend to lower SiO_2 values (75.5 wt%) with lower CaO (down to 0.24 wt%: Fig. 2) in some samples.

Alkali feldspars from the fall deposits and basal ignimbrite are dominantly sanidine but have a significant celsian (Cn) component (Supplementary Fig. 2; Electronic Appendix 2). In the fall deposits they preserve oscillatory zonation where compositions from all zones range over $An_{1–5}Ab_{38–46}Or_{47–58}$ and up to $Cn_{3.7}$. Sanidine also occurs as inclusions in plagioclase, and these sanidine inclusions are in some cases Cn rich (up to $Cn_{5.6}$). Sanidine rims range over $An_{1–3}Ab_{40–46}Or_{51–58}$ and $Cn_{0–2.4}$ but exhibit a bimodality, with clusters of data with <0.35 and 0.4–1 mol% Cn (Fig. 3). Sanidine cores ($Or_{47–58}$ and $Cn_{0–3.6}$) exhibit a greater compositional range than the rims but show a similar bimodal clustering pattern in Cn content to the sanidine rims (Fig. 3). Alkali feldspars from the basal ignimbrite show a greater range in composition ($An_{0–14}Ab_{39–68}Or_{36–59}$) with rare (2.5% of all analyses) anorthoclase ($An_{2–4}Ab_{64–68}Or_{28–32}$) additionally present (Supplementary Fig. 2). Celsian contents in these crystals range up to 10.2 mol% in the cores and 4.1 mol% in the rims (Electronic Appendix 2).

Plagioclases in both the fall deposits and ignimbrite, whether as free crystals or inclusions in sanidine, are dominantly oligoclase ($An_{13–31}Ab_{62–77}Or_{5–15}$: Supplementary Fig. 2) and homogenous, but rare more calcic zones ($An_{43–48}Ab_{49–53}Or_2$) are also found ($<2\%$ of all analyses:

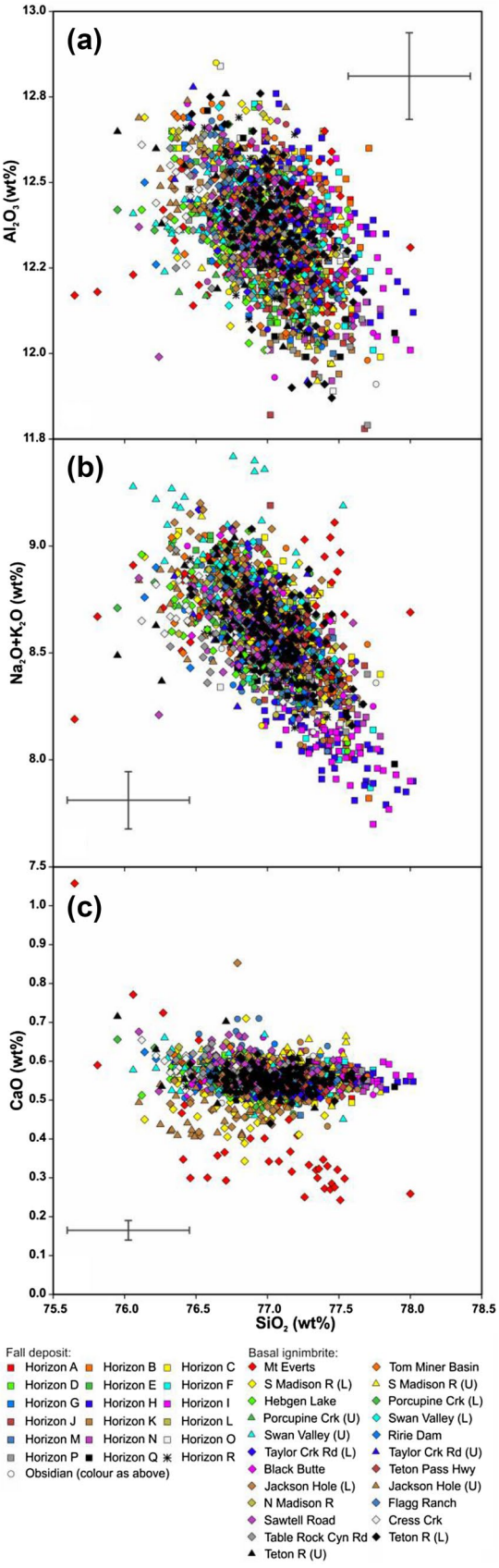

Fig. 2 Major element plots of fall glass, obsidian pyroclasts and basal ignimbrite glass. There is minimal variation with SiO_2 in **a** Al_2O_3 or **b** Na_2O+K_2O but glass from the basal ignimbrite at some localities shows depletions in CaO (**c**). The negative correlation of alkalis and alumina with SiO_2 is consistent with the crystallisation of feldspar. Error bars are 1 sd analytical uncertainties

Electronic Appendix 2). The basal ignimbrite samples also include calcic anorthoclase ($An_{12–18}Ab_{60–65}Or_{17–24}$) in 15% of analyses.

Trace element compositions of glassy materials

In glassy material from the fall deposits and basal ignimbrite, concentrations of incompatible trace elements such as Rb (164–362 ppm) and U (5–12 ppm) show coherent variations (Electronic Appendix 1). If these variations result from crystallisation differentiation, they indicate up to ~ 60% fractional crystallisation (Fig. 4) from the least- to most-evolved glasses, using the partition coefficients of Lu et al. (1992) and Anderson et al. (2000). Trace element ratios indicative of the degree of melt evolution (e.g. Ba/Rb, Sr/Rb) also show lineages that trace back to the least-evolved glass compositions (Fig. 5).

However, within the fall deposits, samples of glass shards and obsidian fragments show compositional clustering in certain elements [e.g. Ba, Sr, light rare earth elements (LREE): Fig. 5a]. Individual glass and obsidian fragments are homogenous in composition based on multiple analyses on the same shard, with any intra-shard variation limited to the range of the respective compositional cluster. Several of the horizons sampled contain glass and obsidian from more than one compositional group. There is more compositional variation within the obsidian fragments (predominantly in Ba concentrations) than the glass shards, possibly due to microlite growth and/or partial hydration, but they fall within the same broad groups. The cluster with the lowest Ba (10–30 ppm) is LREE depleted relative to the other clusters (Fig. 5; Table 1) and has the lowest Sr/Rb ratio (down to 0.004; equivalent to Rb/Sr of up to 250). Variations in LREE concentrations are consistent with the effects of fractionation of trace amounts of chevkinite, identified through qualitative EPMA analysis. The other clusters are distinguishable in Ba concentration (33–65; 90–175; >360 ppm) but have overlapping LREE ranges (e.g. La: Fig. 5). Trace element compositions of glass selvedges on sanidine crystals from selected fall deposit horizons show a compositional range (e.g. 19–369 ppm Ba) but have similar clustering to that seen in the matrix glass (Fig. 6). Lower Ba glass selvedge compositions are dominantly found coating low Cn (< 0.35 mol%) sanidine rims (Fig. 6).

Glass compositions from the basal ignimbrite samples extend the range observed in the fall deposits to higher Ba

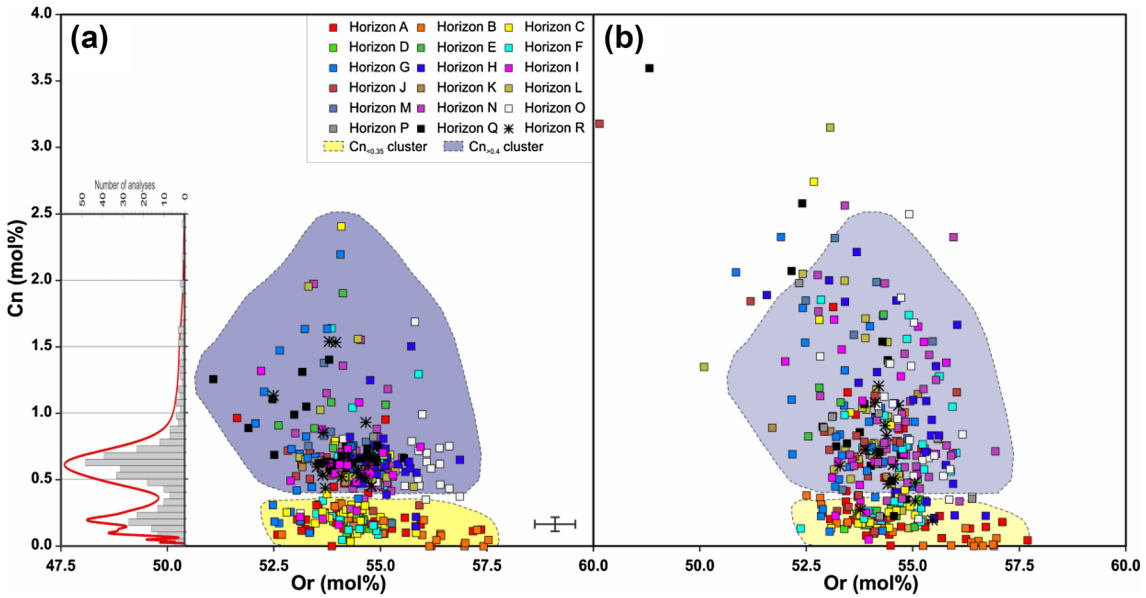

Fig. 3 **a** Sanidine rim compositions in the fall deposit showing the presence of two clusters, one with < 0.35 mol% Cn (yellow highlight) and a higher Cn cluster (> 0.4 mol%: purple highlight), based on the bimodality of rim compositions seen in a histogram of rim compositions (inset; bin widths are 0.05 mol% Cn). The red curve is a probability density function generated using Isoplot (Ludwig 2008), plotted with the average 2 sd of 22% for BaO analyses in sanidine. Cluster colours are based on glass selvedge compositions and the link to fall glass clusters (see Supplementary Fig. 2 and text for details). **b** Sanidine core compositions. The fields of rim compositions from panel **a** are copied here to show the comparative ranges in compositions. Error bars in the bottom right corner of **a** show 2 sd analytical uncertainties

(890 ppm) but continue to show clustering (Fig. 5c), including replicating those compositional clusters represented in the fall deposit data. These clusters form a coherent overall evolutionary trend between the fall deposit compositions and the least-evolved glass in the basal ignimbrite (Fig. 5d). Glass shards sampled from any one ignimbrite sample contain compositions falling into multiple clusters, analogous to what is seen in individual stratigraphic horizons from the fall deposit.

Thermometry calculations

We used the Elkins and Grove (1990) two-feldspar thermometer in conjunction with major element analyses of plagioclase inclusions in sanidine (and vice versa) to calculate feldspar crystallisation temperatures. Feldspar compositions were normalised on a Cn-free basis. Feldspars from all but two fall deposit horizons (E and O) had suitable inclusions and yielded temperature estimates from 768 to 855 °C with a mean and median of 819 °C (Fig. 7; Electronic Appendix 2). The temperature estimates from the basal ignimbrite show a greater range (768–918 °C) and extend to higher temperatures, with a mean of 832 °C and a median of 843 °C.

For comparison, zircon saturation temperatures were calculated for the matrix and obsidian glasses. Calculated temperatures from the fall deposit yield ranges of 782–838 °C with a mean of 815 °C, and 733–803 °C with a mean of 776 °C using the calibrations of Watson and Harrison (1983) and Boehnke et al. (2013), respectively (Fig. 7; Electronic Appendix 1). Zircon saturation temperatures calculated from basal ignimbrite glasses extend to hotter temperatures with a range of 783–878 °C and a mean of 823 °C, and 733–851 °C with a mean of 784 °C, respectively, using the same calibrations. We note that here, as in other studies where alternative estimates of magma temperature are available (e.g. Barker et al. 2014), the calibration of Watson and Harrison (1983) yields temperature estimates that are closely comparable, whereas the Boehnke et al. (2013) calibration yields values that are consistently lower than with other methods. We were unable to further investigate this disparity by comparing our results with Fe–Ti oxide thermometry, due to the exsolved nature of one or both minerals in oxide pairs.

Plagioclase–melt hygrometer

The plagioclase–melt hygrometer of Waters and Lange (2015) was used to estimate melt H_2O concentrations. Given the uniformity of major element glass compositions within each fall horizon sampled (Fig. 2), an average glass composition for each horizon was used for the melt composition, coupled with a mean pressure of 200 MPa (after Myers et al. 2016). However, pressure has little effect on the

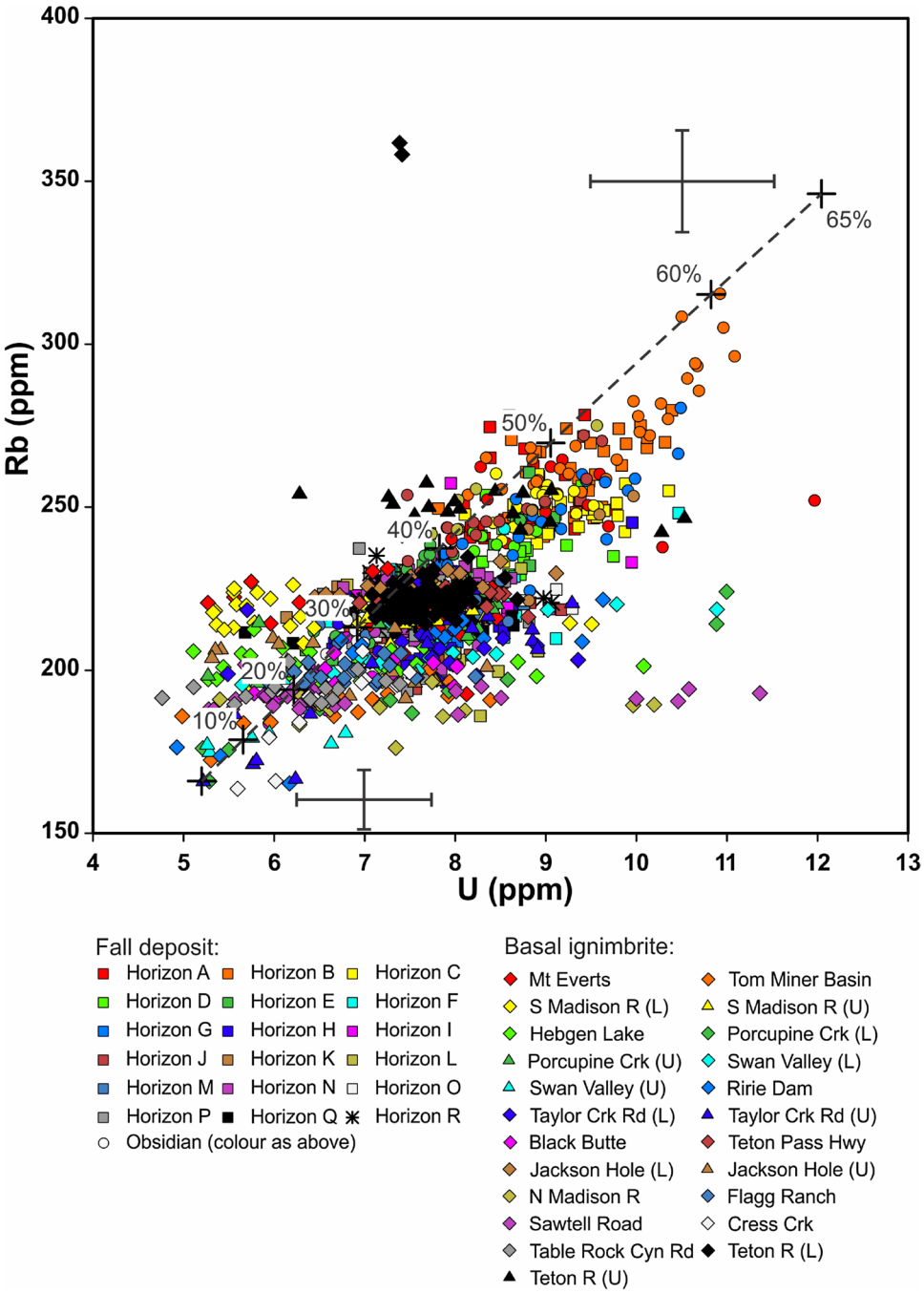

Fig. 4 Fractional crystallisation modelling of the range in glass shard compositions analysed in this study. Partition coefficients of $D_U = 0.2$ and $D_{Rb} = 0.3$ are used (from Lu et al. 1992 and Anderson et al. 2000, respectively) to model the range in fractional crystallisation across the observed range in compositions. Error bars show projected 2 sd analytical uncertainties based on error slope regression at the relevant concentrations (see supplementary material)

hygrometer: for example, adoption of the lowest restored pressure of 80 MPa from Myers et al. (2016) only changes the hygrometry estimates by 0.03 wt% H_2O. Using the mean two-feldspar thermometry model temperature for each horizon, the corresponding calculated H_2O contents in samples from the fall deposits range from 3.2 to 4.5 wt% (Electronic Appendix 2). These values are similar to the estimates of 3.2–4.9 wt% H_2O based on melt inclusion data (Myers et al. 2016).

Given that plagioclase–melt hygrometer results for the fall samples are consistent with H_2O estimates from melt inclusions, we apply this hygrometer method to basal ignimbrite samples for which H_2O concentrations are otherwise unknown. Again using mean model temperatures from each locality, the hygrometer yields H_2O contents of 2.4–4.5 wt%, with one outlier at 1.4 wt% reflecting a single feldspar pair from the basal ignimbrite at Mt. Everts that yielded an estimate of 918 °C.

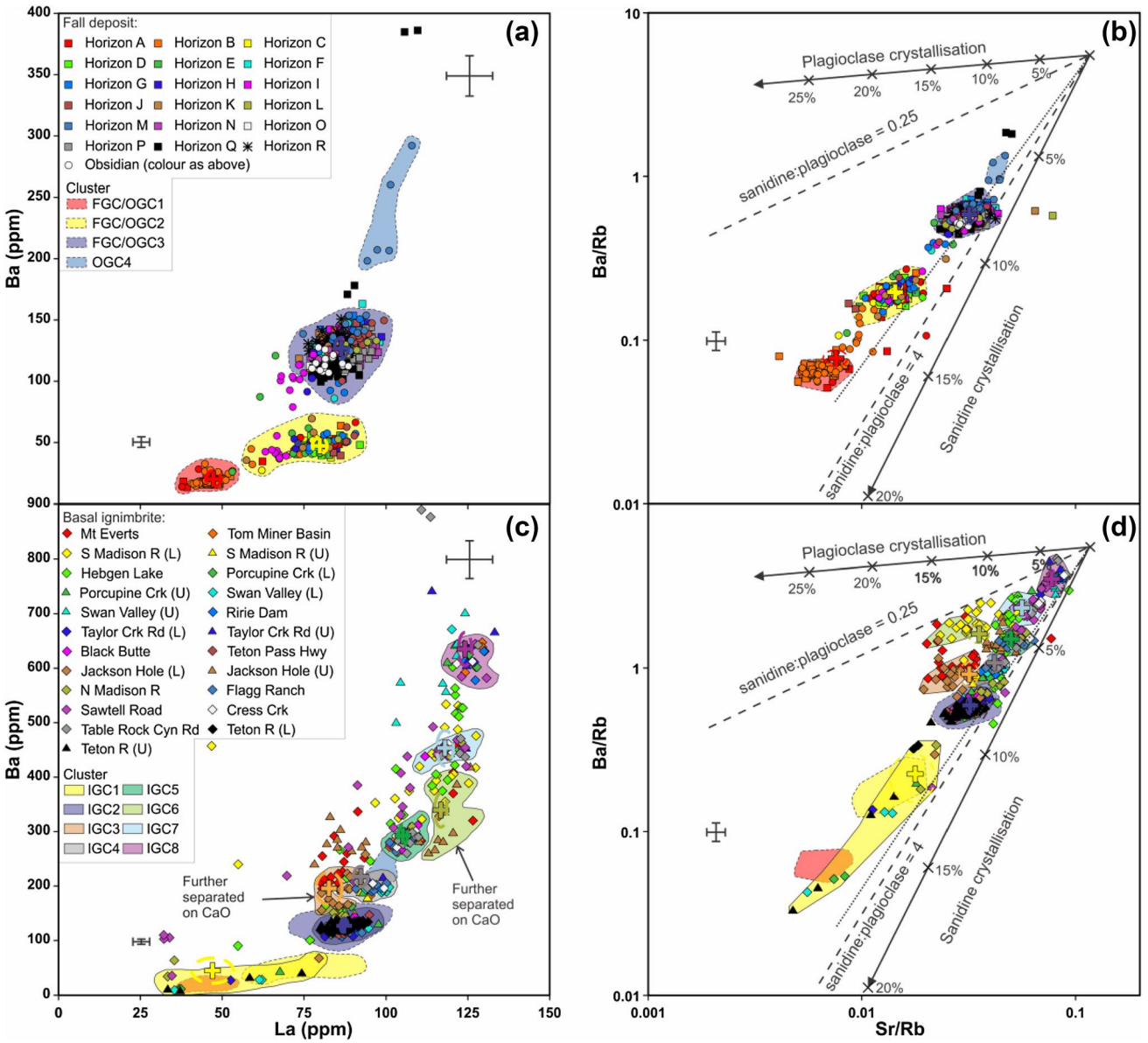

Fig. 5 **a** Plot of Ba vs La abundances in glass shards and obsidian pyroclasts from the fall deposits showing the grouping of four clusters, identified using cluster analysis (colours as in Supplementary Fig. 3). **b** Ba/Rb vs Sr/Rb ratios for the samples plotted in **a** and the corresponding cluster fields. Solid lines indicate sense and magnitude (degrees in wt%) of exclusively plagioclase and sanidine crystallisation from a starting value that represents the least-evolved composition measured in this study. Dashed lines reflect crystallisation of a mineral assemblage with 4:1 ratios of the two feldspars. Dotted line is best fit through the least-evolved ends of each cluster and has a slope of 1.68, which corresponds to a sanidine:plagioclase ratio of 1.7. **c** Plot of Ba vs La concentrations in glassy material from the basal ignimbrite. Fields of clusters in panel **a** are copied here for comparison. In addition, fields showing the eight compositional clusters identified by cluster analysis in the basal ignimbrite are shown. **d** Ba/Rb vs Sr/Rb ratios for basal ignimbrite glass compositions. Cluster fields are copied from **b** and supplemented by fields denoting the dominant region of each cluster in the basal ignimbrite. Solid and dashed crystallisation lines are as in **b**. Dotted line represents a best fit line through each of the basal ignimbrite clusters and has a slope of 2.1, consistent with crystallisation of an assemblage with a sanidine:plagioclase ratio of 3. Large crosses indicate the mean for each cluster and dashed ellipses show 95% confidence about the mean. Error bars show projected 2 sd analytical uncertainties based on error slope regression at the relevant concentrations (see supplementary material)

Table 1 Mean composition for selected elements and the intra-cluster variation (2 sd in italics) in the fall deposits (glass shards and obsidian clasts) and basal member A ignimbrite

	FGC1		FGC2		FGC3		OGC1		OGC2		OGC3		OGC4			
SiO_2	77.28	*0.2*	77.10	*0.3*	77.12	*0.3*	77.12	*0.3*	77.08	*0.2*	77.09	*0.2*	76.80	*0.2*		
TiO_2	0.08	*0.0*	0.05	*0.0*	0.09	*0.0*	0.08	*0.0*	0.08	*0.0*	0.09	*0.0*	0.12	*0.0*		
Al_2O_3	12.43	*0.1*	12.33	*0.2*	12.32	*0.2*	12.38	*0.2*	12.36	*0.1*	12.36	*0.1*	12.41	*0.1*		
FeOt	1.23	*0.0*	1.33	*0.1*	1.39	*0.1*	1.25	*0.1*	1.35	*0.1*	1.40	*0.1*	1.51	*0.0*		
CaO	0.56	*0.0*	0.54	*0.0*	0.56	*0.0*	0.54	*0.0*	0.56	*0.0*	0.56	*0.0*	0.66	*0.0*		
Na_2O	3.43	*0.2*	3.47	*0.2*	3.34	*0.2*	3.53	*0.2*	3.43	*0.1*	3.37	*0.1*	3.30	*0.2*		
K_2O	4.96	*0.1*	5.15	*0.2*	5.13	*0.1*	5.05	*0.1*	5.09	*0.1*	5.08	*0.1*	5.15	*0.1*		
Ti	456	*40*	501	*30*	598	*39*	449	*42*	498	*31*	583	*48*	708	*39*		
Rb	265	*9*	245	*7*	219	*7*	271	*18*	246	*14*	222	*15*	214	*4*		
Sr	1.77	*0.4*	3.43	*0.5*	6.91	*0.9*	2.22	*0.7*	3.47	*0.5*	6.58	*0.8*	9.22	*0.6*		
Y	103	*6*	97	*5*	87	*5*	99	*6*	96	*7*	86	*7*	82	*4*		
Zr	176	*11*	220	*9*	218	*11*	180	*16*	216	*15*	215	*16*	241	*12*		
Nb	72	*3*	69	*2*	61	*2*	73	*5*	68	*5*	61	*4*	61	*2*		
Ba	18	*2*	47	*5*	128	*18*	23	*8*	48	*6*	121	*18*	233	*37*		
La	46	*3*	81	*4*	87	*4*	49	*7*	79	*6*	84	*7*	100	*5*		
Ce	95	*4*	158	*6*	166	*7*	102	*15*	154	*12*	160	*14*	191	*10*		
Yb	9.93	*1.0*	9.44	*1.0*	8.43	*0.9*	9.91	*0.9*	9.17	*0.9*	8.32	*0.9*	8.17	*0.5*		
Pb	47.60	*1.8*	45.29	*2.6*	40.60	*2.2*	47.25	*4.1*	43.89	*3.8*	40.94	*4.3*	49.78	*4.9*		
Th	33.03	*2.1*	34.82	*2.0*	31.67	*2.0*	33.39	*3.4*	34.24	*3.4*	31.54	*3.1*	31.12	*1.9*		
U	9.29	*0.6*	8.93	*0.6*	7.64	*0.5*	9.61	*0.9*	8.76	*0.9*	7.49	*0.7*	6.99	*0.4*		
	IGC1		IGC2		IGC3		IGC4		IGC5		IGC6		IGC7		IGC8	
SiO_2	77.09	*0.3*	77.03	*0.2*	77.08	*0.3*	76.86	*0.3*	76.79	*0.3*	76.66	*0.3*	76.68	*0.3*	76.48	*0.2*
TiO_2	0.04	*0.0*	0.06	*0.0*	0.06	*0.0*	0.05	*0.1*	0.05	*0.1*	0.07	*0.1*	0.08	*0.1*	0.10	*0.1*
Al_2O_3	12.41	*0.2*	12.36	*0.2*	12.29	*0.2*	12.39	*0.2*	12.41	*0.1*	12.43	*0.1*	12.35	*0.1*	12.40	*0.1*
FeOt	1.23	*0.1*	1.33	*0.1*	1.31	*0.2*	1.42	*0.1*	1.52	*0.1*	1.65	*0.1*	1.58	*0.2*	1.74	*0.1*
CaO	0.55	*0.1*	0.55	*0.0*	0.46	*0.1*	0.55	*0.0*	0.57	*0.0*	0.44	*0.0*	0.58	*0.1*	0.61	*0.0*
Na_2O	3.43	*0.2*	3.43	*0.2*	3.32	*0.2*	3.37	*0.2*	3.43	*0.2*	3.30	*0.2*	3.41	*0.2*	3.44	*0.1*
K_2O	5.24	*0.2*	5.22	*0.2*	5.46	*0.2*	5.34	*0.2*	5.23	*0.1*	5.43	*0.1*	5.30	*0.2*	5.22	*0.1*
Ti	451	*49*	608	*23*	591	*45*	652	*35*	736	*26*	864	*51*	856	*59*	952	*46*
Rb	215	*21*	219	*15*	219	*29*	205	*12*	197	*7*	213	*10*	198	*12*	185	*14*
Sr	3.64	*1.9*	6.90	*0.6*	6.75	*1.4*	8.42	*1.7*	9.70	*1.1*	7.37	*1.8*	10.84	*2.4*	14.06	*1.2*
Y	103	*6*	88	*3*	84	*5*	82	*4*	80	*3*	72	*3*	74	*3*	72	*2*
Zr	182	*21*	219	*7*	211	*9*	226	*13*	255	*7*	286	*19*	292	*19*	327	*23*
Nb	75	*4*	63	*2*	63	*3*	61	*2*	60	*1*	57	*2*	57	*2*	55	*1*
Ba	45	*34*	127	*11*	196	*72*	220	*43*	293	*25*	339	*53*	453	*56*	635	*75*
La	47	*16*	87	*3*	82	*10*	92	*5*	105	*3*	117	*5*	118	*6*	124	*5*
Ce	102	*28*	167	*5*	162	*16*	179	*8*	201	*7*	223	*8*	225	*10*	234	*7*
Yb	10.53	*1.0*	8.46	*0.6*	8.19	*0.9*	8.06	*0.8*	7.70	*0.7*	7.00	*0.7*	7.28	*0.7*	7.07	*0.6*
Pb	48.90	*2.9*	41.53	*2.8*	46.13	*6.5*	42.58	*5.3*	38.05	*2.1*	38.44	*1.6*	39.76	*8.7*	37.87	*10.1*
Th	35.48	*2.5*	31.48	*1.4*	31.21	*1.7*	30.52	*1.6*	30.68	*1.2*	29.66	*1.0*	29.97	*1.4*	29.10	*1.4*
U	9.92	*0.9*	7.82	*0.5*	7.85	*0.7*	7.37	*0.5*	6.65	*0.4*	5.98	*0.3*	5.98	*0.4*	5.51	*0.3*

Cluster labels are from Fig. 5. Major and minor element oxides in wt%, trace elements in ppm

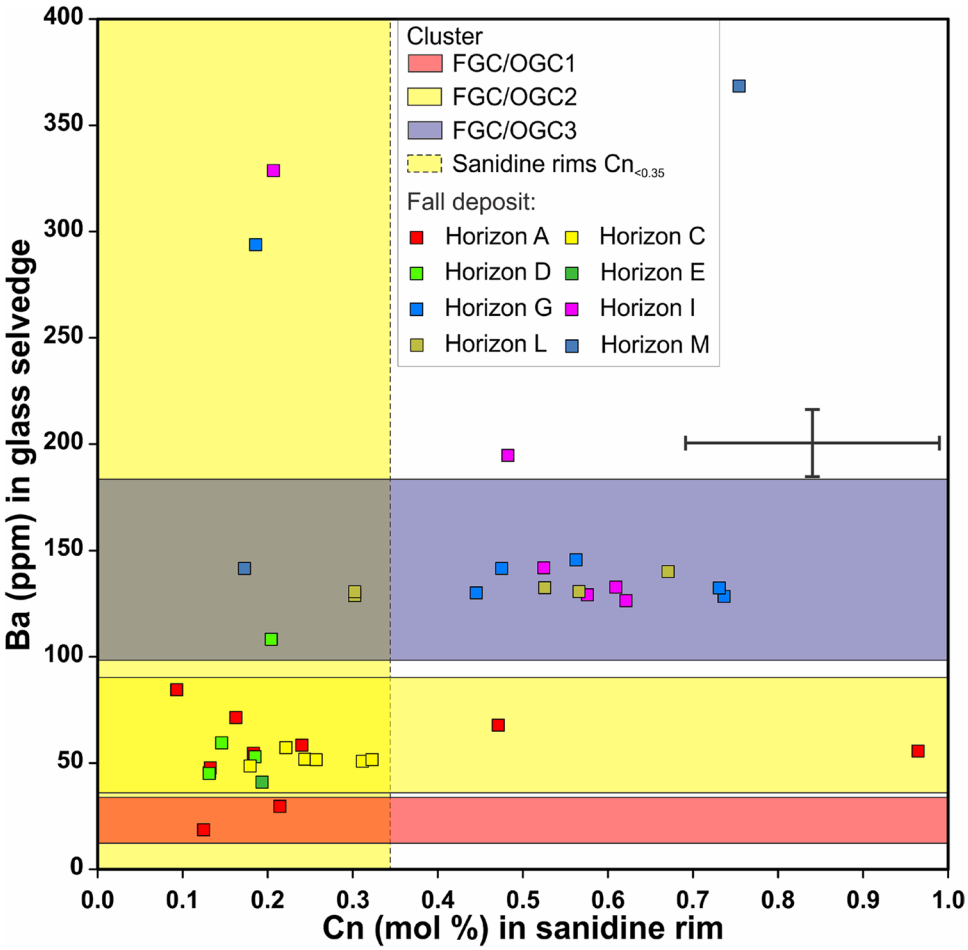

Fig. 6 Glass selvedge Ba compositions plotted relative to their adjacent sanidine rim celsian component (Cn) from selected fall deposit horizons (Electronic Appendix 1 + 2). Shaded regions show the compositional ranges of the glass clusters (solid outline) and low Cn sanidine rim cluster (dashed outline). Colour coding as in Figs. 3 and 5. The data indicate that the low Cn sanidine cluster (see Fig. 3) is associated with FGC1 and 2 (Fig. 5). The clustered sanidine compositions (Fig. 3) suggest that FGC1 and 2 emanated from a distinct upper-level magmatic lineage, separate from the magmatic lineage with higher Cn sanidines associated with FGC3. Error bars represent 2 sd analytical uncertainties. Ba error bar derived for 200 ppm through error slope regression (see supplementary material for details)

Discussion

Clustering of melt compositions: controls and significance

To quantify the degree of compositional clustering and determine the dominant processes responsible, principal component analysis (PCA) and Bayesian mixture-modelling cluster analysis (MMCA) were conducted using R® (R Development Core Team 2016). PCA works by analysing correlations between elements in a dataset to select the minimum number of variables that constitute the overall compositional variation present. These calculations were conducted independently for the fall deposit glass, fall deposit obsidian and basal ignimbrite glass, using 16 selected elements that show the greatest degree of clustering (Ca measured as CaO, Ti, Rb, Sr, Y, Zr, Nb, Ba, La, Ce, Pr, Nd, Ta, Th, U). Significant principal components (PCs), i.e. the components that extract more variance, or inertia, than a randomly generated broken stick model (Jackson 1993), represent 47% (PCs 1−3), 68% (PCs 1 + 2) and 69% (PCs 1 + 2) of the variance in the fall deposit glass, obsidian and basal ignimbrite glass compositions, respectively (Supplementary Fig. 3; full importance of components is detailed in Electronic Appendix 3). PCA results indicate that the primary control on compositional variation is the compatibility of elements in the crystallising mineral assemblage. This conclusion is supported by the variations in Ba, Sr, LREE, Ti and Zr (notably compatible in the crystallising HRT minerals: sanidine, plagioclase, chevkinite, Fe–Ti oxides and zircon, respectively), driving the bulk of the variance in the dataset and plotting antithetically to incompatible elements (e.g. Rb, Nb, U: Supplementary Fig. 3). An alternative possibility is that the variations are due to mixing (for which, however, there is no evidence on macro- or microscopic scales) of a common initial melt composition with variable amounts of a high- or low-Ba assimilant (e.g. mafic magma, country rock). However, mixing between two end members is more likely to generate a continuum of glass compositions, rather than the clustered pattern observed (Fig. 5). Furthermore, magma mixing commonly generates multi-modal crystal major element compositions (e.g. Streck and Grunder 1999), not what is observed here, particularly in the fall deposit (Supplementary Fig. 2). Also, why mafic magma would be expected to infiltrate such upper levels of the HRT magmatic system or why rhyolitic melts with similar, cool temperatures would

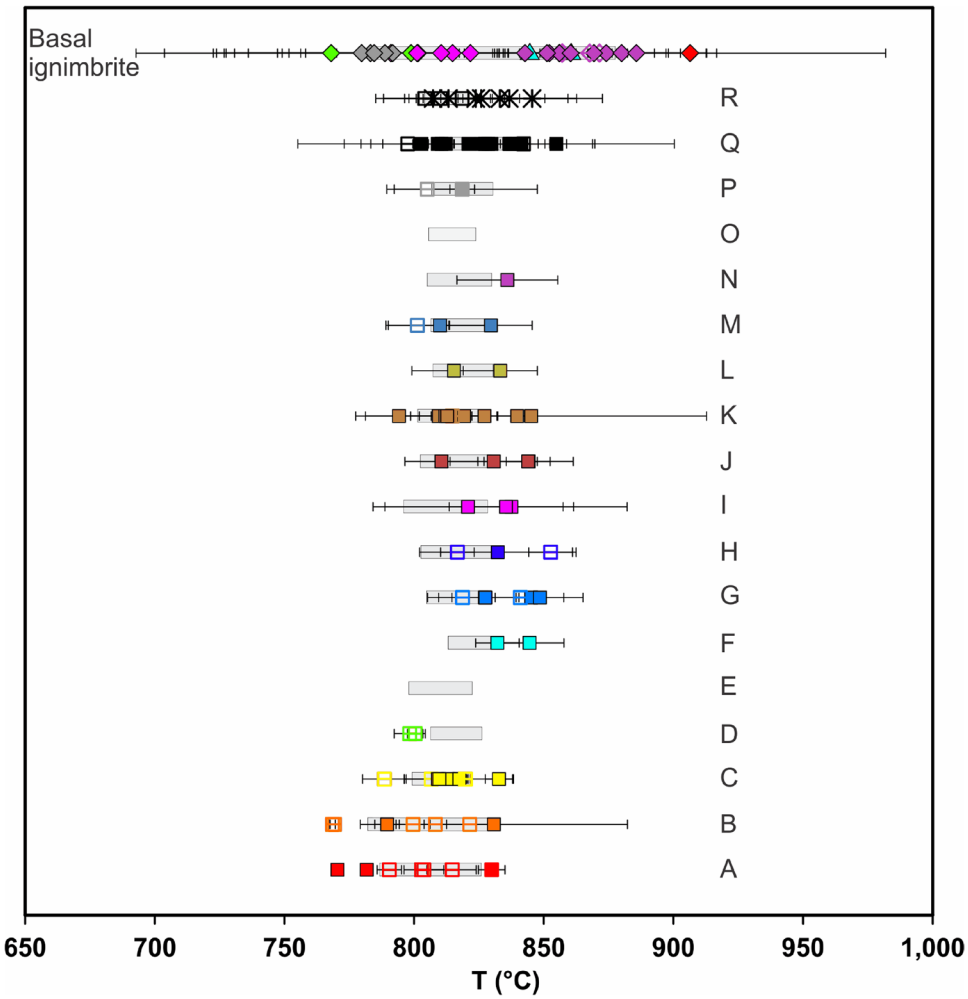

Fig. 7 Temperature estimates using two-feldspar thermometry (Elkins and Grove 1990) through the fall deposits at the Mount Everts location (lettered levels: see Fig. 8 for stratigraphic log) and into the basal ignimbrite at multiple locations (Fig. 1). Data point colours as in Fig. 5. Filled symbols show sanidine inclusions in plagioclase, open symbols indicate plagioclase inclusions in sanidine. No suitable inclusions were found in horizons E and O. Shaded grey bars show the range in zircon saturation temperatures calculated from glass and obsidian compositions using the calibration of Watson and Harrison (1983)

assimilate variable amounts of country rock is puzzling. We, therefore, propose that the observed compositional variation is predominantly related to variations in the degree of fractional crystallisation.

The MMCA, using only significant principal components, distinguishes five clusters in the PCA of the fall glass compositions (labelled FGC1 to FGC5, ordered by their Ba concentrations: Supplementary Fig. 3a). However, three of these (clusters three to five) have overlapping 95% confidence ellipses in all significant principal components and are hereafter treated as one cluster (FGC3). Six clusters are distinguished by MMCA in obsidian clasts from the fall deposit (Supplementary Fig. 3b). Based on overlapping 2 sd confidence ellipses, we combine obsidian clusters 1 and 5 into one (hereafter OGC1), and 3 and 6 into another (hereafter OGC3). These combined clusters in turn show similarity in compositions (overlapping means at the 1 sd level: Table 1) to FGC1 and FGC3, respectively. Another independent cluster (OGC4) is discerned by MMCA but is a minor component (0.5% of fall deposit glassy material) relative to the others. The compositions of clusters FGC–OGC 1–3 identified in this study correspond within error to those associated with the eruptive clusters 1–3, respectively, proposed by Myers et al. (2016) based on the compositions of reentrants (unsealed melt inclusions) in quartz phenocrysts. Therefore, like Myers et al. (2016), we interpret each cluster to represent a melt-dominant domain that is physically separate, as there is no evidence of mingling between different cluster compositions. In the fall deposit, FGC–OGC 3 is dominant, comprising 76% of analysed glassy material (glass shards and obsidian).

MMCA of the basal ignimbrite samples yields eight distinguishable compositional clusters (correspondingly labelled IGC1-8), but some of these have partially overlapping 2 sd confidence ellipses (Supplementary Fig. 3c). IGC1 (4% of basal ignimbrite analyses) is notable for comprising compositions that span the ranges of FGC–OGC 1 and 2, and therefore represents two of the melt-dominant domains tapped during fall deposition. IGC2 overlaps within 1 sd of FGC–OGC 3 (Table 1) and is also the dominant basal ignimbrite cluster (46% of analyses: Fig. 5). The compositional similarities and proportions of the relevant

shards in the basal ignimbrite samples indicate that the magma bodies that vented to feed the fall deposits were still being evacuated at the onset of widespread ignimbrite deposition, rather than these shards representing surficial pickups. Furthermore, some sparsely present, less-evolved glass compositions in the fall deposits (e.g. OGC 4: 0.5% of analyses), are replicated in the basal ignimbrite as clusters IGC4 and 5 (collectively 21% of analyses). This observation suggests that OGC4 represents early erupted material of those clusters that were evacuated in greater proportions during ignimbrite generation. Although previously unrecognised (cf. Myers et al. 2016), they are identified here probably due to a larger number of glass shards being analysed relative to those of unsealed melt inclusions. All clusters are statistically significant, indicated by the discrete means and 95% confidence ellipses (Fig. 5) determined through standard error slope regression (see supplementary material and Supplementary Fig. 4).

The clustered nature of glass compositions in the fall deposits and basal ignimbrite suggests that the HRT magmatic system was not a unitary, continuously zoned or homogenous magma body, but rather consisted of multiple discrete domains. The absence of significant intra-shard heterogeneity also suggests that there was limited mixing between these domains at depth or within shallow conduits, and that the domains remained distinct upon evacuation (cf. Mahood et al. 1985; Streck and Grunder 1997; Aguirre-Díaz 2001). However the trace element compositional variations within each cluster, oblique to the overall trend (Fig. 5), imply that each domain itself underwent some degree of melt compositional evolution following its isolation. We infer a fractional crystallisation control on the compositional variations observed within and between individual clusters, as indicated by the association of element eigenvectors in the PCA (Supplementary Fig. 3) and variously sloped inter- and intra-cluster trends (Fig. 5).

Modelling of compositional trends

Crystallisation modelling was performed to explore the significance of the observed inter- and intra-cluster rends. Because plagioclase and sanidine are co-crystallising, we consider the concentrations of feldspar-compatible Ba and Sr. The relationship between Ba and Sr will be controlled by their differing partition coefficients (e.g. Ba more compatible in sanidine) and by the proportion of plagioclase to sanidine crystallisation. Assuming constant bulk partition coefficients, expected due to the uniform major element compositions (Supplementary Fig. 2), linear slopes should result from the logarithmic relationship between Ba and Sr if fractional crystallisation is the dominant control. We use Ba/Rb and Sr/Rb ratios, rather than Ba and Sr concentrations, to minimise analytical scatter. In addition, as Rb is very incompatible in the HRT mineral assemblage, it will have contrasting behaviour to Ba and Sr with fractional crystallisation leading to greater variation in the ratios relative to elemental concentrations. Algebraic manipulation of the Rayleigh fractionation differential equation gives

$$\delta \log(\mathrm{Ba}) = (D_{\mathrm{Ba}} - 1)\delta \log f,$$

where f is the mass fraction of melt remaining and D_{Ba} is the partition coefficient of Ba. This subsequently yields the equation expressing the changes in the respective ratios related to their partition coefficients:

$$\frac{\delta \log(\mathrm{Ba/Rb})}{\delta \log(\mathrm{Sr/Rb})} = \frac{(D_{\mathrm{Ba}} - D_{\mathrm{Rb}})}{(D_{\mathrm{Sr}} - D_{\mathrm{Rb}})}.$$

Partition coefficients of 28.4, 11.3 and 0.08 for Ba, Sr and Rb, respectively, in sanidine were used and a coefficient of 0.08 for Rb in plagioclase (from Anderson et al. 2000 and references therein). In plagioclase, partition coefficients of 1.33 and 10.60 for Ba and Sr, respectively, were used, calculated using the parameterisations of Blundy and Wood (1991) at An_{20} and 820 °C (the average plagioclase composition and two-feldspar temperature estimates, respectively, for the combined fall deposit and basal ignimbrite datasets).

Bulk partition coefficients were calculated for different ratios of plagioclase to sanidine crystallisation (ignoring the minor effect of other phases on the relevant coefficients) to model feldspar crystallisation and compare against inter- and intra-cluster trends. Starting compositions of 900, 163 and 19 ppm for Ba, Rb and Sr, respectively, were used, determined from the least-evolved concentrations of each element in this dataset. Joining the least-evolved (i.e. highest Sr/Rb and Ba/Rb) points of FGC–OGC 1–3 results in a slope with a gradient of 1.68 ($r^2 = 0.99$), which could be generated by a sanidine:plagioclase ratio of 1.7 (Fig. 5b). Similarly, a trend connecting the least-evolved ends of IGC 1,2,4,5,7, and 8 has a slope of 2.01 ($r^2 = 0.99$), which can be replicated through crystallisation of an assemblage with a sanidine:plagioclase ratio of 3 (Fig. 5d). Intra-cluster trends, although with weaker constraints, have shallower slopes of 0.72, 0.4 and 0.59 for FGC–OGC 1, 2 and 3 ($r^2 = 0.52$, 0.24, 0.32), respectively, that could reflect a lower sanidine:plagioclase ratio of < 0.2.

The linear compositional trends observed in log–log plots (Fig. 5) indicate a fractional crystallisation control on the subtle chemical differences observed between the clusters. This modelling further suggests that although the overall trend (across all clusters) in the glass compositions can be explained by a sanidine-dominant crystallising assemblage, the intra-cluster trends suggest a plagioclase-dominant assemblage (Fig. 5). The simplest explanation for

this contrast arises from the experimental results of Almeev et al. (2012). The early separation of the melt-dominant bodies (demonstrated by the bimodal compositions of sanidine cores and rims: Fig. 3) means that their compositions diverge along chemical trends driven by higher temperature, sanidine-dominant crystal fractionation. Once separated, each body then evolved with lowering temperatures, with increased proportions of plagioclase in the crystallising assemblage. However, the relative proportions of sanidine and plagioclase are also dependent on H_2O contents, and so the changes in crystallisation assemblages may also in part reflect coupled temperature and H_2O activity variations, with decreased activity favouring plagioclase crystallisation (e.g. Wilke et al. 2017). The clusters characterised by lower CaO (IGC3 + 6) in particular may reflect prolonged plagioclase-dominant crystallisation (Fig. 5d). This distinctive combination of characteristics implies the presence of a complex magmatic system consisting of multiple, individually diverse melt-dominant bodies within a larger-scale compositionally heterogeneous system.

Pre-eruptive state of the Huckleberry Ridge magmatic system

Thermometry and hygrometry calculations applied to the initial deposits of the HRT indicate that significant variations in temperature and H_2O concentration were present in the upper parts of a complex HRT magmatic system prior to early evacuation. Here we present combined two-feldspar and Watson and Harrison (1983) zircon saturation temperatures to reconstruct the temperature conditions in these upper parts.

Model temperatures range from 768 °C in the earliest erupted material to > 900 °C in the basal ignimbrite (which, however, still represents an 'early' stage in the overall eruption). Increasing calculated model temperatures are correlated with increased sanidine Cn component and inversely correlated with Or content, implying that the temperature calculations genuinely represent a pre-eruptive variability across the melt-dominant bodies. Although a Cn component in the sanidine was not included in the original experiments of Elkins and Grove (1990), we note that almost the full range (768–871 °C) of two-feldspar model temperatures are represented in pairs with < 1 mol% Cn (Fig. 7). Furthermore, an upper limit of model temperatures in the fall deposit samples of 854 °C is also consistent with the upper limit of stability for sanidine at 2 kbar and 4 wt% H_2O in experimental studies (Almeev et al. 2012). The similarity between two-feldspar temperature estimates and zircon saturation temperatures (Fig. 7; Watson and Harrison 1983) also supports the temperature estimates from sanidines with a broad range of Cn compositions. Melt H_2O contents inferred using the Waters and Lange (2015) hygrometer decrease with height in the fall deposits. Although the plagioclase hygrometer is strongly temperature dependent, within our estimated temperature range it yields values consistent with the Myers et al. (2016) data for melt inclusions, which also indicated an overall decrease in magmatic H_2O contents up-section through the fall deposits.

The distinctive Cn compositions of the alkali feldspars from clusters FGC1 + 2 and FGC3 allow us to investigate whether the different melt-dominant compositional domains had different temperatures. Temperatures calculated from plagioclase inclusions in sanidines that had rims with $Cn_{<0.35}$ (i.e. FGC1 + 2) range from 768 to 820 °C with a mean of 789 °C. In comparison, temperatures calculated from sanidines with $Cn_{>0.4}$ (i.e. FGC3) range from 798 to 853 °C with a mean of 819 °C. The presence of lower, but overlapping, temperatures associated with FGC1 + 2 is also consistent with zircon saturation temperatures. Temperatures calculated from FGC–OGC 1 are the lowest, with a range of 782–826 °C and a mean and median of 798 °C. Glass and obsidian from FGC–OGC 2 yield temperatures from 796 to 830 °C with a mean and median of 816 °C, which overlap those calculated from FGC–OGC 3 glass and obsidian (797–838 °C with a mean and median of 817 °C).

The cooler, but overlapping nature of temperatures obtained from lower Cn sanidines and glass from FGC–OGC 1, suggests that there were modest (up to ~ 20–30 °C) temperature differences between the different melt-dominant bodies. However, this lower temperature, more-evolved glass compositional group (FGC–OGC 1), is associated with higher restored pressures (142–189 MPa, based on H_2O and CO_2 solubility in melt inclusions from quartz population 1 of Myers et al. 2016, compared to the total range of 85–204 MPa). This observation indicates that there is not a simple temperature–depth–melt evolution relationship in the HRT magmatic system as would be expected with a single, coherent magma body (cf. Bishop Tuff: Wallace et al. 1999; Hildreth and Wilson 2007).

The HRT magma body: configuration and early evacuation

Systematic sampling of glassy material through the fall deposits and basal ignimbrite at multiple localities around three sides of the HRT caldera allows for temporal and spatial reconstruction of evacuation during the opening eruptive stages. Our data show that three magmatic domains were systematically and sequentially evacuated through the fall deposits (Fig. 8), consistent with and extending the findings of Myers et al. (2016). Although there was a hiatus in evacuation of compositional groups FGC–OGC1 and FGC–OGC2 in the upper parts of the fall deposits, these groups then reappear in the basal ignimbrite collectively as IGC1. The similar trends in abundance of low Cn sanidines and glassy

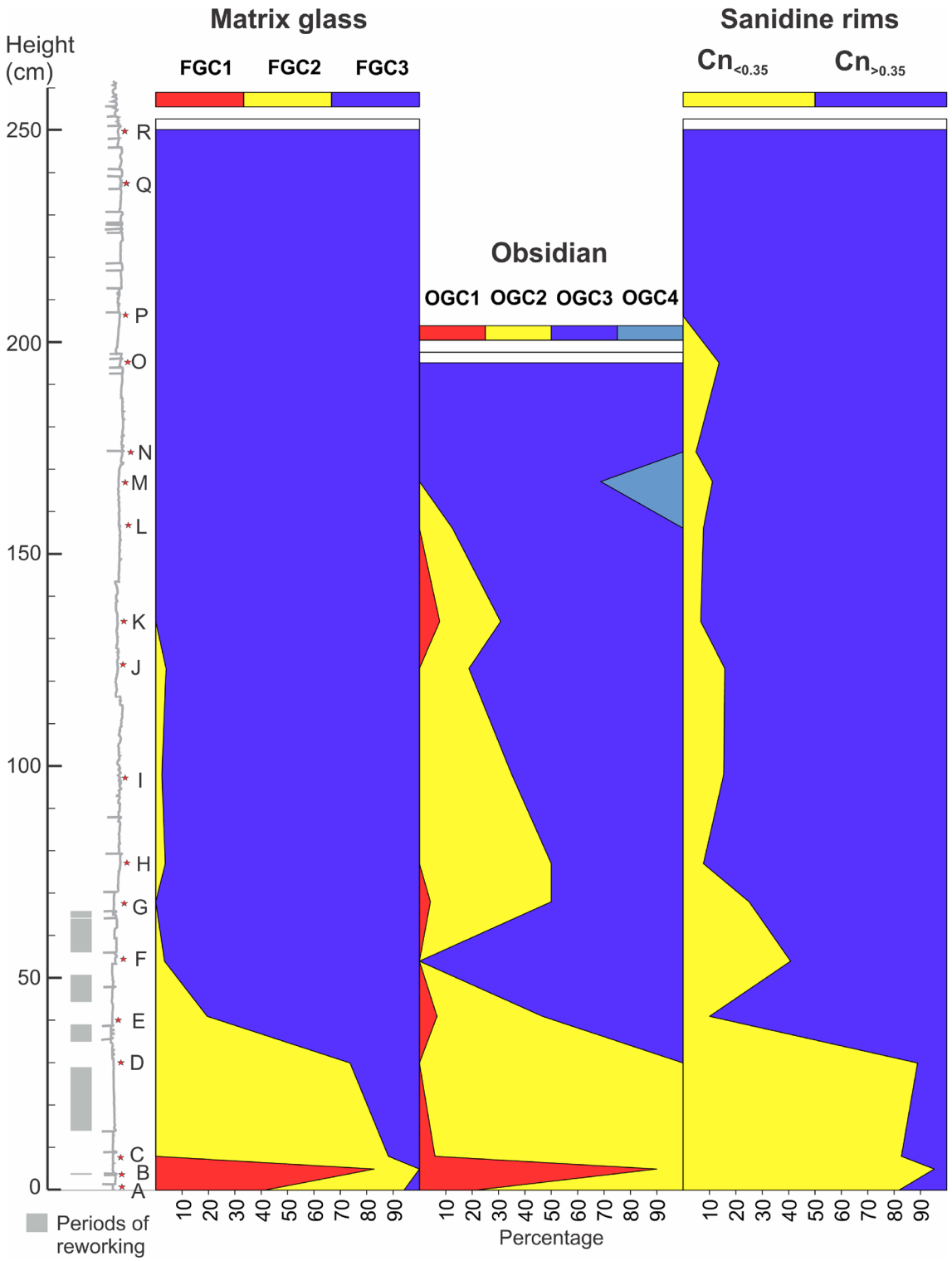

Fig. 8 Comb diagram showing the changes in proportions of the compositional groupings of matrix glass, obsidian pyroclasts and sanidine rims through the fall deposit sequence at Mt. Everts. Colours of the groupings in the 'glass' and 'obsidian' column match those of the fields in Fig. 5 and the sanidine rim compositions of Fig. 3. A schematic stratigraphic log of the Mt. Everts section is shown, along with the horizons sampled. See Supplementary Fig. 1 for a photograph of the sampled section

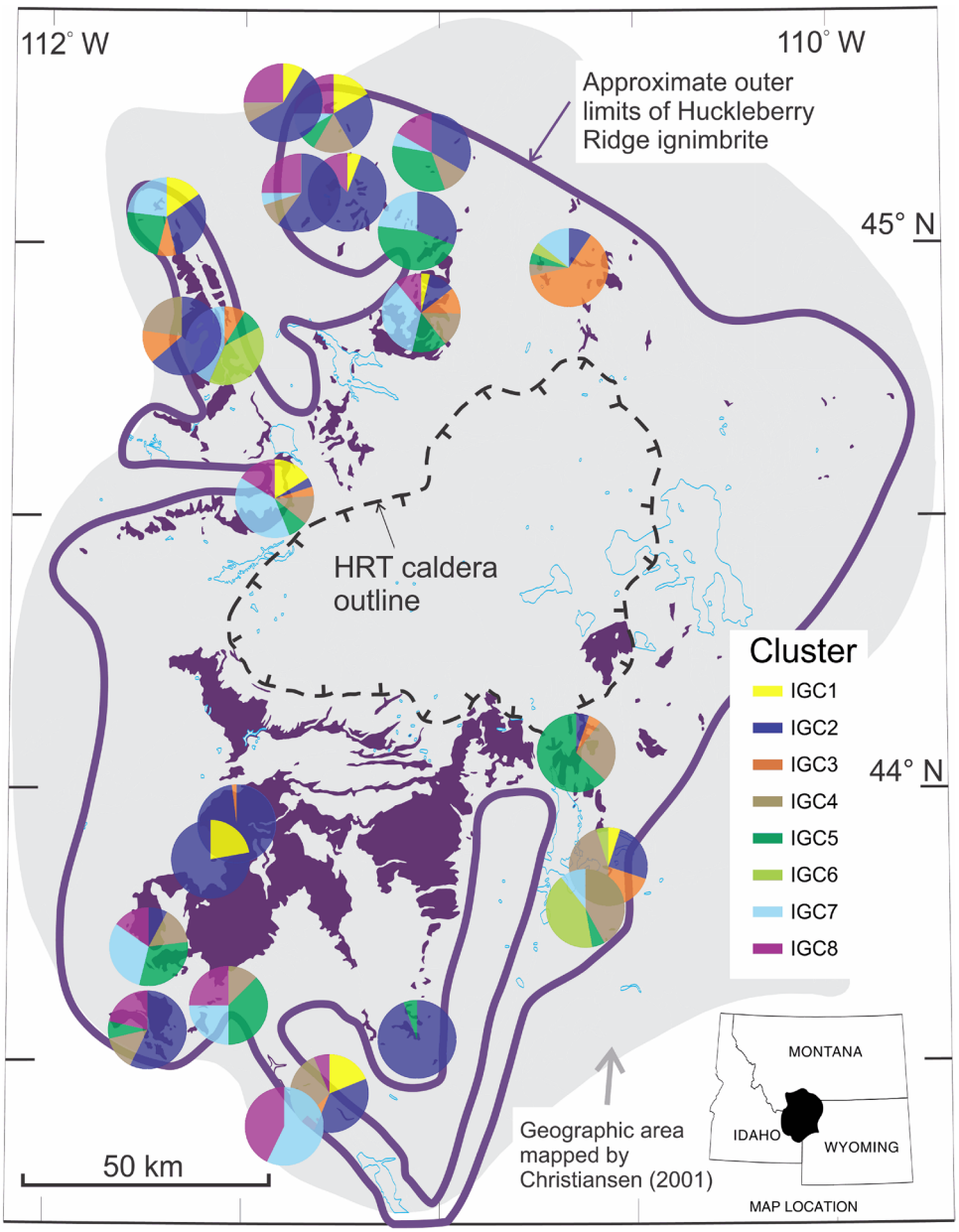

Fig. 9 Pie charts showing the relative abundances of different clusters in basal ignimbrite glass compositions at each sample locality (see Fig. 1 for location names. Colours as in Supplementary Fig. 2c). Where samples were collected from multiple levels at the same location, pie charts overlap. No strong sectorial or proximal-to-distal (i.e. temporal) patterns to glass compositions in the basal ignimbrite are evident

material from clusters FGC–OGC1 + 2 further support their link, as inferred from glass selvedge analyses (Fig. 6).

When considered by locality, basal ignimbrite A samples show that multiple compositional clusters are present in samples in all directions around and distances from the caldera rim (Fig. 9), with no clear patterns. On this basis, we infer that material from a greater number of melt-dominant bodies was simultaneously incorporated into the earliest widespread ignimbrite-forming flows when compared with the fall deposits. This, plus the preservation of fall sequences with broadly similar overall stratigraphy beneath the full extent of the ignimbrite, implies two things. First, that the onset of continuous ignimbrite deposition was effectively synchronous at all localities studied here. Second that the fall-to-flow transition must have been accompanied both by an escalation in eruption rates and a sharp increase in the number of magma bodies evacuated.

Determining the configuration and state of the magmatic system(s) is important in understanding the nature and magnitude of internal stresses (e.g. buoyancy) present during the onset of eruption. It is therefore important to consider whether the individual HRT melt-dominant bodies, each with their own internal compositional variability, existed as discrete isolated domains or were instead sills forming part of a larger interconnected magma reservoir (cf. Tarasewicz et al. 2012; Cashman and Giordano 2014). In the latter case, temporal trends are observed that have been related to tapping of different levels within a sill-dominated magmatic

system. In contrast, the absence of any temporal trend in glass compositions in the basal HRT ignimbrite A (i.e. a systematic change from proximal to distal localities: Fig. 9) suggests that the bodies were predominantly laterally, rather than vertically separated, and were tapped collectively at the onset of ignimbrite deposition. Additional constraints come from restored entrapment pressures (storage depths) from melt inclusions (Myers et al. 2016) in quartz populations 5 + 6 (upper fall) that are compositionally equivalent (high Ba, low CaO of population 5) to matrix glass only observed by us in the basal ignimbrite (IGC6: Table 1). These restored entrapment pressures indicate depths as shallow (85–160 MPa: ~ 3–6 km depth), if not shallower, than those of the three magma domains tapped during the earliest fall deposit stages (106–204 MPa: ~ 4–8 km depth). We interpret these data to indicate that at least some of the magma bodies tapped at the onset of ignimbrite-forming activity were laterally separated from, and in some cases at shallower depths than, those that fed the fall deposit (rather than beneath them). Furthermore, two-feldspar and zircon saturation temperature estimates in basal ignimbrite samples overlap with those of the fall deposits, precluding a significant increase in temperature being associated with the melt-dominant bodies tapped at the onset of ignimbrite deposition (Fig. 7).

The clustered nature of the glass shard, obsidian clast and sanidine rim compositions in the fall deposits and basal ignimbrite in turn raise questions about whether the multiple melt-dominant bodies reflect extracts from a common root zone, or were derived from two (or more) adjacent root zones. The clustering observed in sanidine rim compositions is mirrored in the core compositions (Fig. 3), implying that the melt bodies became physically separated and chemically distinct prior to the onset of sanidine crystallisation. This onset is estimated to be at ≥ 850 °C, based on our two-feldspar thermometry (Fig. 7) and published experimental work (Almeev et al. 2012). The low Cn sanidine group is linked to FGC1 and FGC2 through glass selvedge analyses (Fig. 6) and comparable changes in sanidine rim, glass and obsidian cluster proportions through the fall deposits (Fig. 8). These observations imply that the separation between FGC1 + 2 and FGC3 occurred prior to the last ~ 50 °C of cooling and crystallisation, based on the temperature range determined from low Cn sanidines. This inference is in turn consistent with the quartz-hosted melt-inclusion compositional patterns (Myers et al. 2016), as the onset of quartz crystallisation is inferred to occur at a lower temperature than that of sanidine (Almeev et al. 2012). Of the quartz grains that contained a re-entrant and a melt inclusion studied by Myers et al. (2016), only one has a re-entrant from their eruptive cupolas 1 or 2 (equivalent to our FGC1/2) and a melt inclusion

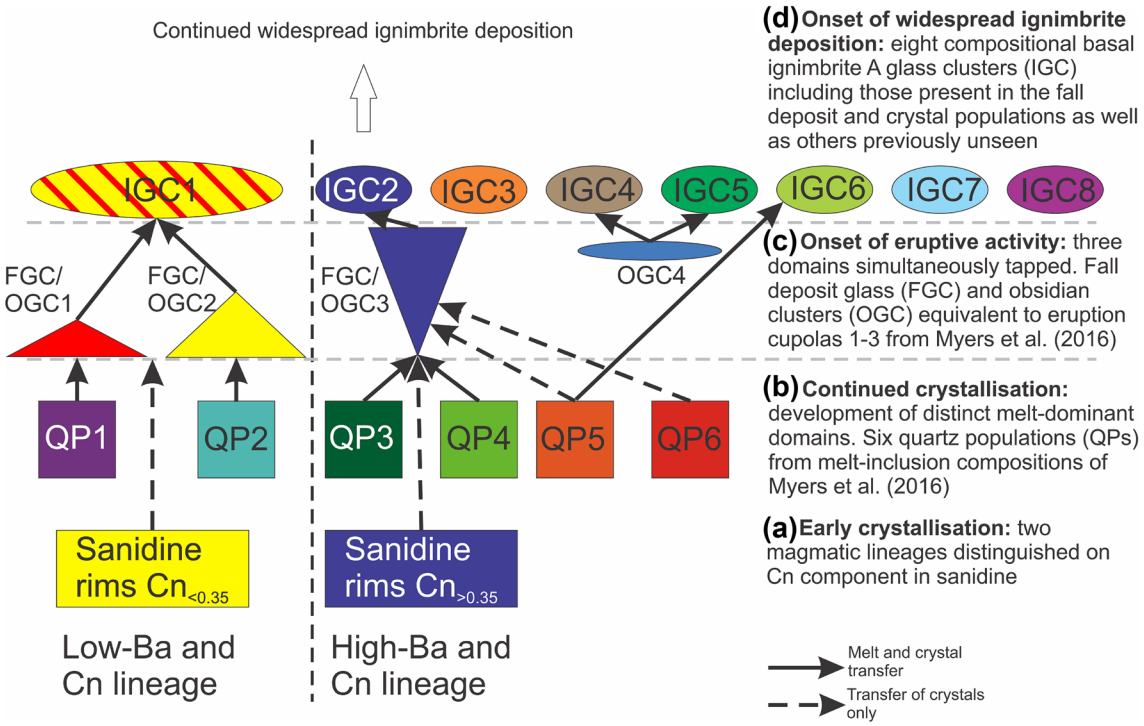

Fig. 10 Schematic flow diagram showing the relationships and links between the clusters inferred from **a** sanidine rim compositions (this study), **b** quartz populations based on melt-inclusion analyses (Myers et al. 2016), **c** fall deposit glass shard and obsidian clast compositional characteristics (Myers et al. 2016 and this study) and **d** basal ignimbrite glass compositions

from another cluster, indicating also that there was chemical and physical separation of these bodies prior to the co-crystallisation of quartz and sanidine.

Myers et al. (2016) found that some quartz-hosted melt-inclusion compositions from the fall deposits (their quartz populations 5 + 6) did not correspond to compositions of the melt-dominant domains active during generation of the fall deposits studied by them. However, the low CaO, higher Ba melt-inclusion composition of quartz population 5 is replicated in glass from the basal ignimbrite (IGC6: Table 1). Single quartz grains that hosted melt inclusions from multiple populations always contained glass compositions that linked to quartz populations 5 or 6 and 3 + 4 types, the latter of which is comparable to our FGC–OGC3. These observations indicate that there was some exchange of crystals between the domains which hosted quartz populations 5 + 6 (i.e. IGC6) and FGC–OGC3 after the onset of quartz crystallisation (Fig. 10).

The separation of low-Ba melt bodies (represented by FGC1 + 2) prior to sanidine crystallisation and the interchange of quartz crystals between melt-bodies tapped only by the ignimbrite and FGC3 suggests there are two distinct larger scale magmatic lineages (i.e. two compositionally independent entities) present in the HRT magmatic system and tapped in these early stages of the HRT (Fig. 10). The first is characterised by the low Cn sanidines that are present in FGC1 and FGC2 and the second is associated with the higher Cn sanidines linked to FGC3. From these two lineages were developed multiple cupolas, each of which developed its own distinctive traits in melt composition and which were systematically tapped in the opening stages (Fig. 10). The term 'cupolas' was used to describe these bodies by Myers et al. (2016) as their focus on only the earliest erupted material precluded an insight into the relation of these bodies to the larger magmatic system(s). With our extended dataset, we can show that these domains, representing two melt-dominant lineages, persist through into the onset of basal ignimbrite deposition. We, however, retain the use of 'cupola' as their relationship to the overall HRT magmatic system(s) requires geochemical investigation of the volumetrically dominant later-erupted material (Swallow et al. manuscript in preparation). Complexity in the HRT magma system has previously been discerned in the overall chemical and isotopic characteristics of the ignimbrite units (Doe et al. 1982; Hildreth et al. 1984, 1991; Bindeman et al. 2008; Wotzlaw et al. 2015). However, these documented complexities apply over much larger time and length scales, involving volumes of magma that are 1–3 orders of magnitude larger than those detailed in our study. The subtle variations we see at the start of the HRT eruption have not previously been discerned.

The complex magma system configuration and episodic style of eruption onset shown by the HRT is not unique within the Yellowstone-Snake River Plain volcanic province (Ellis et al. 2013) and also has analogues worldwide, particularly in New Zealand (e.g. Gravley et al. 2007; Allan et al. 2012, 2017; Cooper et al. 2012, 2016; Bégué et al. 2014; Cashman and Giordano 2014; Pistolesi et al. 2016). Many of these examples involved magma systems distributed beneath geographic areas that are smaller than that encompassed by the mapped HRT caldera (Christiansen 2001). Available data do not, however, permit us to outline the specific areas involved in the initial development of HRT caldera collapse. However, the complexities represented by the individual cupolas in the HRT have not been observed before and would escape notice unless trace element data and thermobarometric estimations are considered together using material derived from high-resolution, stratigraphically constrained sampling.

Implications for eruption behaviour

The presence and complex evacuation of multiple melt-dominant bodies is not readily incorporated in the variety of numerical models used to investigate the onset of large silicic eruptions (e.g. Jellinek and DePaolo 2003; Gregg et al. 2012, 2015; Caricchi et al. 2014; Degruyter and Huber 2014; Malfait et al. 2014). Jellinek and DePaolo (2003) highlight a contrasting model behaviour between smaller magma bodies that are expected to generate sufficient overpressure to cause dike propagation and hence erupt, versus large bodies that heat the wall rocks sufficiently to suppress dike propagation. Furthermore, small systems are predicted to be triggered in a different manner to larger systems, with a greater emphasis on internal processes in smaller systems (Gregg et al. 2015). The HRT magma body appears to fit both model end members, with multiple compositionally and physically discrete melt-dominant domains capping the larger scale overall magmatic system beneath what became the overall HRT caldera (Fig. 11). This configuration would result in a significantly different stress fields when compared to a single large magma body and has important thermo-mechanical implications. For example, if one or more smaller scale melt-dominant bodies were tapped then this could serve to change the stress state in the upper crust, and thereby destabilise adjacent bodies and influence the rate of any decline in overpressure in the system, potentially prolonging the time before caldera collapse (Gudmundsson 2012; Bégué et al. 2014).

Our reconstruction for the HRT system yields further implications. Magmatic systems composed of multiple smaller melt-dominant domains rather than a single continuous magma body require different conditions to survive at shallow depths in the crust. Smaller bodies will cool more rapidly, and therefore require either greater thermal inputs into the overall magmatic system, or are subject to shorter

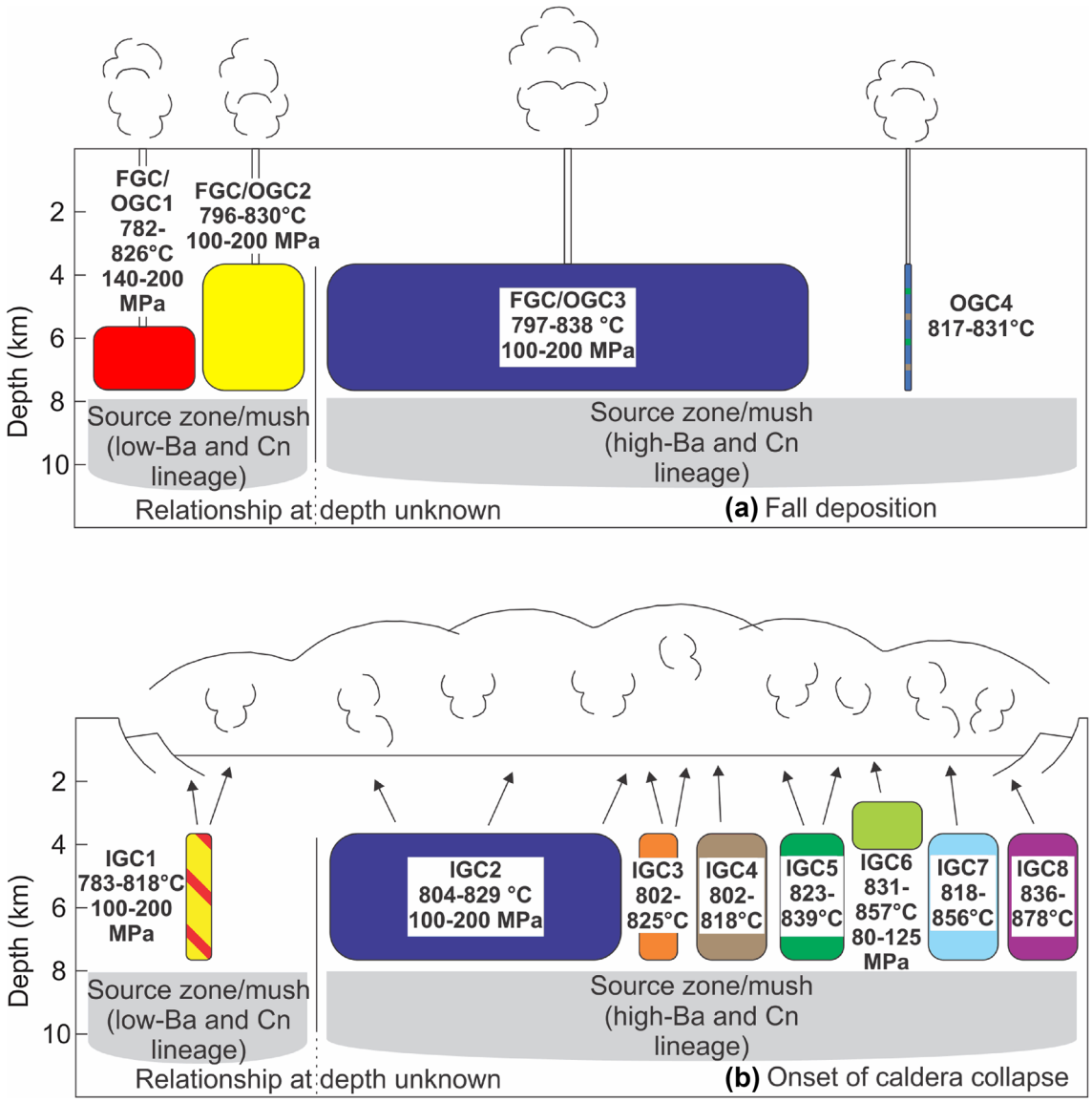

Fig. 11 Schematic diagram showing the configuration of the tapped magma domains **a** at the onset of fall deposition, and **b** at the onset of caldera collapse and deposition of ignimbrite member A. The HRT magmatic system tapped in these stages of the eruption is inferred to consist of multiple discrete, laterally adjacent melt-dominant bodies representing two magmatic lineages. Three bodies (FGC–OGC 1–3: Fig. 10) were erupted at the onset of fall deposition (Fig. 8). Eight compositional clusters, representing nine melt-dominant bodies (IGC1 represents two bodies, FGC–OGC1 + 2), including the three tapped during fall deposition, were simultaneously evacuated following caldera collapse at the onset of ignimbrite deposition. The sizes of the rectangles representing the melt-dominant bodies are in proportion to the numerical abundance of analyses assigned to that cluster within each data set. Temperatures are from zircon saturation thermometry (Watson and Harrison 1983) and cupola pressures, where given, are derived from melt inclusion volatile contents from the relevant cluster (Myers et al. 2016). The melt-dominant bodies with unknown storage depths are assumed to be laterally adjacent at depths equivalent to ~ 100–200 MPa

lifespans as bodies of eruptible magma. Thus, the potential existence of small (i.e. short-lived) melt-dominant bodies has important implications for monitoring. Although the Yellowstone magmatic system is currently thought to contain melt in average proportions too low to permit eruption (Huang et al. 2015 and references therein), current resolution levels of geophysical imaging techniques are too coarse to define small (< ~ 10 km wide) bodies with higher proportions of melt that could potentially be erupted (Lowenstern et al. 2006).

The simultaneous tapping of multiple melt-dominant cupolas at the start of the HRT eruption (Figs. 8, 10), the eruptive hiatuses observed in the fall deposits, and the highly variable and unusually slow pre-eruption magma ascent rates inferred from melt inclusion data have been used to infer that an external rather than an internal mechanism

triggered the eruption onset (Myers et al. 2016). An alternative view for the compositional diversity is from the work by Cashman and Giordano (2014) who argue that multiple distinct melt domains can be tapped by one conduit from a variety of depths. As previously discussed, however, the absence of mixing in glass and obsidian shards between the various compositional clusters and the overlapping restored entrapment pressures (Myers et al. 2016) suggest that multiple vents were active, tapping three broadly laterally adjacent (not vertically arrayed) magma cupolas during the fall activity.

The transition from fall deposits into basal ignimbrite in the HRT is marked by an increase in the range of melt compositions and number of inferred compositional groupings from four to eight, representing melt-dominant domains evacuated during the onset of widespread ignimbrite deposition (Fig. 10). The inferred increase in eruption rate and involvement of such diverse melt domains imply that this transition is associated with the onset of roof instability and the beginning of caldera collapse. The transition followed the evacuation of roughly 50 km^3 of magma (minor, when compared to the total ~ 2500 km^3 erupted: Christiansen 2001). This estimate is based on available isopach data from the fall deposits below the ignimbrite (CJNW, unpublished data) and assuming that the magma volume is one-third that of the bulk fall deposits. Evacuation of a portion of the magma chamber leading to underpressure has long been proposed as a means of inducing caldera collapse (e.g. Roche and Druitt 2001). Important to note is the reappearance in the basal ignimbrite of glass compositions similar to FGCs 1 + 2, which are absent from the middle to upper parts of the fall deposits. This observation indicates that the vent areas and feeder cupolas for FGCs 1 + 2, which were active briefly at the eruption onset (Fig. 8), were reactivated during the onset of ignimbrite activity, further consistent with onset of caldera collapse.

The continuingly clustered nature of glass compositions in the basal ignimbrite indicates also that caldera collapse was probably not due to the over-pressurisation of a single larger, deeper melt-dominant body. Such a scenario would be expected to yield a more coherent, unitary glass compositional array (cf. Chamberlain et al. 2015). Christiansen (2001) proposed that the overall HRT caldera is a composite structure resulting from collapses associated with each of the three ignimbrite packages. However, we infer that the caldera collapse associated just with the onset of ignimbrite A is in itself a composite structure, incorporating multiple vent locations.

Comparisons and contrasts

The combination of features we and Myers et al. (2016) describe from the Huckleberry Ridge Tuff make it without a direct comparator. Notable variations and clustering in erupted melt compositions are known from other ignimbrite-forming events, but such occurrences have typically been interpreted to represent sampling of compositional zones or gradients within a unitary chamber (e.g. Mahood et al. 1985; Fridrich and Mahood 1987; Schuraytz et al. 1989; Aguirre-Díaz 2001; Kaneko et al. 2007), rather than tapping of discrete magmatic bodies. At an extreme, the 7.05 Ma, 280 km^3 Rattlesnake Tuff has a visually spectacular diversity of juvenile components, which were clustered into five groups by Streck and Grunder (1997). In this and other examples, though, the diversity is evident in pumice and shard colours and reflected in wide ranges in major element abundances. In contrast, the major element variations in the HRT glasses studied here are barely larger than analytical uncertainties, and there are no colour variations that can be linked to composition.

In turn, the presence of multiple discrete melt dominant bodies has previously been proposed for several eruptions. One is the paired Mamaku–Ohakuri eruptions that exhibit compositional clustering in matrix glass and melt inclusion compositions, inferred to represent a magmatic system composed of multiple smaller melt-dominant bodies (Bégué et al. 2014). However, these events, unlike the HRT, started with a homogenous fall deposit and only following this were other bodies tapped. Another, the 1.0 Ma, ~ 1200 km^3 Kidnappers eruption deposits show, through subtle variations in glass and mineral compositions, that three magma bodies were tapped in overlapping sequence (Cooper et al. 2012, 2016). This sequence matches the opening HRT stages, but the Kidnappers withdrawal dynamics were systematic and the magma bodies concerned were collectively one or more orders of magnitude larger than the cupolas proposed to feed the early HRT. Four glass groups have been proposed on the basis of trace element data to be present in the Youngest Toba Tuff (Westgate et al. 2013). However, all four groups are represented in some single pumice, suggesting that these groups represent large bodies that were in close spatial proximity and spanning the entire multi-thousand cubic kilometre eruption.

Tapping of melts from each of the two magmatic lineages in the early HRT was intermittent. For example, the low Cn sanidine, lower Ba-in-glass, magmatic lineage is present early in the fall deposits (FGC1 + 2), disappears, then reappears in the basal ignimbrite (Fig. 8). A compound 4.3 ka eruption deposit from Campi Flegrei shows the closest match to our inferences from the HRT, with clustering expressed dominantly in trace elements, and with a clear link to multiple vent sites active sequentially and simultaneously (Pistolesi et al. 2016). However, this example is on a volumetrically smaller scale and did not subsequently lead into ignimbrite formation, or subsequent caldera collapse.

The combination of immense overall volume, multiple small-scale definable melt-dominant magma domains and subtlety of the geochemical variations makes the HRT unique. The level of stratigraphic control that we have reveals more detail within the first 2–3% of the eruption volume than is known from any other eruption of this size. Although the transition from fall to widespread ignimbrite deposition is simple, the magma system tapped even at these early stages of the eruption was remarkably complex. The significant trace elemental variations reported here thus represent a challenge for stratigraphically linked correlations of near-source HRT fall deposits and ignimbrite with any equivalent distal tephra deposits (cf. Perkins and Nash 2002).

Conclusions

Detailed geochemical investigations of matrix glass and feldspar in the initial fall deposits and earliest ignimbrite (basal vitric parts of member A) of the HRT show wide variations that form statistically robust clusters. When coupled with depth estimates from H_2O and CO_2 in quartz-hosted melt inclusions these data show that a complex magmatic system was present, reaching to shallow levels (4–8 km depth: Myers et al. 2016) in the crust prior to eruption. Nine compositionally distinct melt-dominant domains are determined from the material studied here, which in turn can be interpreted to represent two distinct magmatic lineages that were evacuated during the opening stages of the HRT eruption. Overlaps in inferred storage depths (Myers et al. 2016), and the presence of the two distinct lineages imply that these melt-dominant domains were spatially separated, predominantly laterally rather than simply being vertically stacked (cf. Cashman and Giordano 2014). The fall deposit sequentially and systematically tapped three of these cupolas at the beginning of the eruption, under conditions inferred to reflect control by an external, tectonic trigger (Myers et al. 2016). The onset of widespread deposition of ignimbrite member A is associated with evacuation of nine melt-dominant domains, including the three bodies that were tapped earlier during fall deposition (Fig. 10). The onset of ignimbrite deposition was broadly synchronous (within the limits of field evidence) from proximal to distal areas in the sectors north, west and south of the final, overall caldera structure (cf. Bishop and Oruanui ignimbrites: Wilson and Hildreth 1997; Wilson 2001). This rapid onset of flow activity, coupled with the diversity of melt groupings represented in all areas sampled in the basal ignimbrite across a 180 degree sector (Fig. 9), is interpreted to mean that caldera collapse began at this early stage (after ~ 50 km^3 of a 2500 km^3 eruption), plausibly due to depressurisation of the magmatic system. Our work shows that, although the physical appearance of the deposits can appear relatively straightforward, high-resolution micro-analytical data can reveal remarkable complexities in large silicic magma systems. Whether the remarkable diversity shown by the Huckleberry Ridge Tuff is unique or turns out to be common awaits the documentation in equivalent detail of other examples.

Acknowledgements Swallow was supported by a Commonwealth Scholarship administered by the Commonwealth Scholarship Commission. Wilson thanks the Yellowstone (YELL-05248) and Grand Teton (GRTE-00604) research offices for permission to work in the respective national parks, Bob Christiansen for his introduction to the Huckleberry Ridge Tuff, and the Royal Society of New Zealand for a James Cook Fellowship and past support under Marsden Fund Grant VUW0813. Additional financial support was provided by National Science Foundation Grant EAR-1524824 to Wallace and a VUW Faculty Strategic Research Grant (209484) to Swallow. We thank Adam Kent, Dan Morgan, Ian Schipper and Dan Sinclair for their help with data collection and processing, and acknowledge Shan de Silva, Guil Gualda, John Stix and an anonymous reviewer for their informative comments that helped improve the manuscript.

References

Aguirre-Díaz GJ (2001) Recurrent magma mingling in successive ignimbrites from Amealco caldera, central Mexico. Bull Volcanol 63:238–251

Allan ASR, Wilson CJN, Millet M-A, Wysoczanski RJ (2012) The invisible hand: tectonic triggering of a rhyolitic supereruption. Geology 40:563–566

Allan ASR, Barker SJ, Millet M-A, Morgan DJ, Rooyakkers SM, Schipper CI, Wilson CJN (2017) A cascade of magmatic events during the assembly and eruption of a super-sized magma body. Contrib Mineral Petrol 172:49

Almeev RR, Bolte T, Nash BP, Holtz F, Erdmann M, Cathey HE (2012) High-temperature low H_2O silicic magmas of the Yellowstone hotspot: an experimental study of rhyolite from the Bruneau–Jarbridge eruptive center, central Snake River Plain, USA. J Petrol 53:1837–1866

Anderson AT, Davis AM, Lu F (2000) Evolution of Bishop Tuff rhyolitic magma based on melt and magnetite inclusions and zoned phenocrysts. J Petrol 41:449–473

Bachmann O, Dungan MA, Lipman PW (2002) The Fish Canyon magma body San Juan volcanic field Colorado: rejuvenation and eruption of an upper-crustal batholith. J Petrol 43:1469–1503

Bachmann O, Deering CD, Lipman PW, Plummer C (2014) Building zoned ignimbrites by recycling silicic cumulates: insight from the 1,000 km^3 Carpenter Ridge Tuff, CO. Contrib Mineral Petrol 167:1025

Bacon CR (1983) Eruptive history of Mount Mazama and Crater Lake caldera Cascade Range, USA. J Volcanol Geotherm Res 18:57–115

Bacon CR, Druitt TH (1988) Compositional evolution of the zoned calcalkaline magma chamber of Mount Mazama, Crater Lake, Oregon. Contrib Mineral Petrol 98:224–256

Barker SJ, Wilson CJN, Smith EGC, Charlier BLA, Wooden JL, Hiess J, Ireland TR (2014) Post-supereruption magmatic reconstruction of Taupo volcano (New Zealand), as reflected in zircon ages and trace elements. J Petrol 55:1511–1533

Bégué F, Deering CD, Gravley DM, Kennedy BM, Chambefort I, Gualda GAR, Bachmann O (2014) Extraction, storage and eruption of multiple isolated magma batches in the paired Mamaku and Ohakuri eruption, Taupo Volcanic Zone, New Zealand. J Petrol 55:1653–1684

Bindeman IN, Fu B, Kita NT, Valley JW (2008) Origin and evolution of silicic magmatism at Yellowstone based on ion microprobe analysis of isotopically zoned zircons. J Petrol 49:163–193

Blundy JD, Wood BJ (1991) Crystal-chemical controls on the partitioning of Sr and Ba between plagioclase feldspar, silicate melts, and hydrothermal solutions. Geochim Cosmochim Acta 55:193–209

Boehnke P, Watson EB, Trail D, Harrison TM, Schmitt AK (2013) Zircon saturation re-revisited. Chem Geol 351:324–334

Caricchi L, Annen C, Blundy J, Simpson G, Pinel V (2014) Frequency and magnitude of volcanic eruptions controlled by magma injection and buoyancy. Nature Geosci 7:126–130

Cas RAF, Wright HMN, Folkes CB, Lesti C, Porreca M, Giordano G, Viramonte JG (2011) The flow dynamics of an extremely large volume pyroclastic flow, the 2.08-Ma Cerro Galan Ignimbrite, NW Argentina, and comparison with other flow types. Bull Volcanol 73:1583–1609

Cashman KV, Giordano G (2014) Calderas and magma reservoirs. J Volcanol Geotherm Res 288:28–45

Chamberlain KJ, Wilson CJN, Wallace PJ, Millet M-A (2015) Microanalytical perspectives on the Bishop Tuff and its magma chamber. J Petrol 56:605–640

Christiansen RL (2001) The Quaternary and Pliocene Yellowstone Plateau volcanic field of Wyoming, Idaho and Montana. US Geol Surv Prof Pap 729-G:G1-G143

Cooper GF, Wilson CJN (2014) Development, mobilisation and eruption of a large crystal-rich rhyolite: the Ongatiti ignimbrite, New Zealand. Lithos 198–199:38–57

Cooper GF, Wilson CJN, Millet M–A, Baker JA, Smith EGC (2012) Systematic tapping of independent magma chambers during the 1 Ma Kidnappers supereruption. Earth Planet Sci Lett 313–314:23–33

Cooper GF, Wilson CJN, Millet M–A, Baker JA (2016) Generation and regeneration of a supervolcanic magmatic system: a case study from Mangakino volcanic centre, New Zealand. J Petrol 57:1135–1170

Degruyter W, Huber C (2014) A model for eruption frequency of upper crustal silicic magma chambers. Earth Planet Sci Lett 403:117–130

Doe BR, Leeman WP, Christiansen RL, Hedge CE (1982) Lead and strontium isotopes and related trace elements as genetic tracers in the upper Cenozoic rhyolite-basalt association of the Yellowstone Plateau volcanic field. J Geophys Res 87:4785–4806

Elkins LT, Grove TL (1990) Ternary feldspar experiments and thermodynamic models. Am Mineral 75:544–559

Ellis BS, Wolff JA, Borough S, Mark DF, Starkel WA, Bonnichsen B (2013) Rhyolitic volcanism of the central Snake River Plain: a review. Bull Volcanol 75:745–763

Fridrich CJ, Mahood GA (1987) Compositional layers in the zoned magma chamber of the Grizzly Peak Tuff. Geology 15:299–303

Gravley DM, Wilson CJN, Leonard GS, Cole JW (2007) Double trouble: paired ignimbrite eruptions and collateral subsidence in the Taupo Volcanic Zone, New Zealand. Geol Soc Am Bull 119:18–30

Gregg PM, de Silva SL, Grosfils EB, Parmigiani JP (2012) Catastrophic caldera-forming eruptions: thermomechanics and implications for eruption triggering and maximum caldera dimensions on Earth. J Volcanol Geotherm Res 241–242:1–12

Gregg PM, Grosfils EB, de Silva SL (2015) Catastrophic caldera-forming eruptions II: the subordinate role of magma buoyancy as an eruption trigger. J Volcanol Geotherm Res 305:100–113

Gudmundsson A (2012) Magma chambers: formation, local stresses, excess pressures, and compartments. J Volcanol Geotherm Res 237–238:19–41

Hildreth W (1981) Gradients in silicic magma chambers: implications for lithospheric magmatism. J Geophys Res 86:10153–10192

Hildreth W, Fierstein J (2012) The Novarupta-Katmai eruption of 1912—largest eruption of the twentieth century: centennial perspectives. US Geol Surv Prof Pap 1791:1–259

Hildreth W, Christiansen RL, O'Neil JR (1984) Catastrophic isotopic modification of rhyolitic magma at times of caldera subsidence, Yellowstone Plateau volcanic field. J Geophys Res 89:8339

Hildreth W, Mahood GA (1986) Ring-fracture eruption of the Bishop Tuff. Geol Soc Am Bull 97:396–403

Hildreth W, Halliday AN, Christiansen RL (1991) Isotopic and chemical evidence concerning the genesis and contamination of basaltic and rhyolitic magma beneath the Yellowstone Plateau volcanic field. J Petrol 32:63–138

Hildreth W, Wilson CJN (2007) Compositional zoning of the Bishop Tuff. J Petrol 48:951–999

Huang H-H, Lin F-C, Schmandt B, Farrell J, Smith RB, Tsai VC (2015) The Yellowstone magmatic system from the mantle plume to the upper crust. Science 348:773–776

Humphreys MCS, Kearns SL, Blundy JD (2006) SIMS investigation of electron-beam damage to hydrous rhyolitic glasses: implications for melt inclusion analysis. Am Mineral 91:667–679

Jackson DA (1993) Stopping rules in principal component analysis: a comparison of heuristical and statistical approaches. Ecology 74:2204–2214

Jellinek AM, DePaolo DJ (2003) A model for the origin of large silicic magma chambers: precursors of caldera-forming eruptions. Bull Volcanol 65:363–381

Kaneko K, Kamata H, Koyaguchi T, Yoshikawa M, Furukawa K (2007) Repeated large-scale eruptions from a single compositionally stratified magma chamber: an example from Aso volcano, Southwest Japan. J Volcanol Geotherm Res 167:160–180

Lowenstern JB, Smith RB, Hill DP (2006) Monitoring super-volcanoes: geophysical and geochemical signals at Yellowstone and other large caldera systems. Phil Trans R Soc Lond A364:2055–2072

Lu F, Anderson AT, Davis AM (1992) Melt inclusions and crystal-liquid separation in rhyolitic magma of the Bishop Tuff. Contrib Mineral Petrol 110:113–120

Ludwig KR (2008) Isoplot/Ex version 3.7. A geochronological toolkit for Microsoft Excel. Berkely Geochronological Centre, Special Publication 4

Mahood GA, Gilbert CM, Carmichael ISE (1985) Peralkaline and metaluminous mixed-liquid ignimbrites of the Guadalajara region, Mexico. J Volcanol Geotherm Res 25:259–271

Malfait W, Seifert R, Petitgirard S, Perrillat JP, Mezouar M, Ota T, Nakamura E, Lerch P, Sanchez-Valle C (2014) Supervolcano eruptions driven by melt buoyancy in large silicic chambers. Nature Geosci 7:122–125

Miller CF, Wark DA (eds) (2008) Supervolcanoes. Elements 4:11–49

Myers ML, Wallace PJ, Wilson CJN, Morter BK, Swallow EJ (2016) Prolonged ascent and episodic venting of discrete magma batches at the onset of the Huckleberry Ridge supereruption, Yellowstone. Earth Planet Sci Lett 451:285–297

Nairn IA, Kohn BP (1973) Relation of the Earthquake Flat Breccia to the Rotoiti Breccia, central North Island, New Zealand. NZ J Geol Geophys 16:269–279

Perkins ME, Nash BP (2002) Explosive silicic volcanism of the Yellowstone hotspot: the ash fall tuff record. Geol Soc Am Bull 114:367–381

Pistolesi M, Isaia R, Marianelli P, Bertagnini A, Fourmentrauz C, Albert PG, Tomlinson EL, Menzies MA, Rosi M, Sbrana A (2016) Simultaneous eruptions from multiple vents at Campi Flegrei

(Italy) highlight new eruption processes at calderas. Geology 44:487–490

R Development Core Team (2016) R: A language and environment for statistical computing R Foundation for Statistical Computing Vienna, Austria. https://www.R-projectorg/

Roche O, Druitt T (2001) Onset of caldera collapse during ignimbrite eruptions. Earth Planet Sci Lett 191:191–202

Rosi M, Vezzoli L, Aleotti P, De Censi M (1996) Interaction between caldera collapse and eruptive dynamics during the Campanian Ignimbrite eruption, Phlegraean Fields, Italy. Bull Volcanol 57:541–554

Schuraytz BC, Vogel TA, Younker LW (1989) Evidence for dynamic withdrawal from a layered magma body: the Topopah Spring Tuff, southwestern Nevada. J Geophys Res 94:5925–5942

Singer BS, Jicha BR, Condon DJ, Macho AS, Hoffman KA, Dierkhising J, Brown MC, Feinberg JM, Kidane T (2014) Precise ages of the Réunion event and Huckleberry Ridge excursion: episodic clustering of geomagnetic instabilities and the dynamics of flow within the outer core. Earth Planet Sci Lett 405:25–38

Singer BS, Costa F, Herrin JS, Hildreth W, Fierstein J (2016) The timing of compositionally-zoned magma reservoirs and mafic 'priming' weeks before the 1912 Novarupta-Katmai rhyolite eruption. Earth Planet Sci Lett 451:125–137

Sparks RSJ, Bursik MI, Carey SN, Gilbert JS, Glaze LS, Sigurdsson H, Woods AW (1997) Volcanic Plumes. John Wiley, Chichester, p 574

Streck ML, Grunder AL (1997) Compositional gradients and gaps in high-silica rhyolites of the Rattlesnake Tuff, Oregon. J Petrol 38:133–163

Streck ML, Grunder AL (1999) Enrichment of basalt and mixing of dacite in the rootzone of a large rhyolitic chamber: inclusions and pumices from the Rattlesnake Tuff, Oregon. Contrib Mineral Petrol 136:193–212

Suzuki-Kamata K, Kamata H, Bacon CR (1993) Evolution of the caldera-forming eruption at Crater Lake, Oregon, indicated by component analysis of lithic fragments. J Geophys Res 98:14059–14074

Tarasewicz J, White RS, Woods AW, Brandsdóttir B, Gudmundsson MT (2012) Magma mobilization by downward-propagating decompression of the Eyjafjallajökull volcanic plumbing system. Geophys Res Lett 39:L19309

Wallace PJ, Anderson AT, Davis AM (1999) Gradients in H_2O, CO_2 and exsolved gas in a large-volume silicic magma system: interpreting the record preserved in melt inclusions from the Bishop Tuff. J Geophys Res 104:20097–20122

Waters LE, Lange RA (2015) An updated calibration of the plagioclase-liquid hygrometer-thermometer applicable to basalts through rhyolites. Am Mineral 100:2172–2184

Watkins JM, Gardner JE, Befus KS (2017) Nonequilibrium degassing, regassing and vapour fluxing in magmatic feeder systems. Geology 45:183–186

Watson EB, Harrison TM (1983) Zircon saturation revisited: temperature and composition effects in a variety of crustal magma types. Earth Planet Sci Lett 64:295–304

Westgate JA, Pearce NJG, Perkins WT, Preece SJ, Chesner CA, Muhammad RF (2013) Tephrochronology of the Toba tuffs: four primary glass populations define the 75-ka Youngest Toba Tuff, northern Sumatra, Indonesia. J Quat Sci 28:772–776

Wilke S, Holtz F, Neave DA, Almeev R (2017) The effect of anorthite and water on quartz-feldspar cotectic compositions in the rhyolitic system and implications for geobarometry. J Petrol 58:789–818

Wilson CJN (2001) The 26.5 ka Oruanui eruption, New Zealand: an introduction and overview. J Volcanol Geotherm Res 112:133–174

Wilson CJN, Hildreth W (1997) The Bishop Tuff: new insights from eruptive stratigraphy. J Geol 105:407–439

Wilson L, Sparks RSJ, Walker GPL (1980) Explosive volcanic eruptions-IV. The control of magma properties and conduit geometry on eruption column behaviour. Geophys J R Astron Soc 63:117–148

Wotzlaw J-F, Bindeman IN, Stern RA, D'Abzac F-X, Schaltegger U (2015) Rapid heterogeneous assembly of multiple magma reservoirs prior to Yellowstone supereruptions. Sci Rep 5:14026